Chapter IX

DESIGN AND SYNTHESIS OF METAL COMPLEXES WITH 2-NAPHTHOIC ACID AND AMINOGUANIDINE: SPECTROSCOPIC CHARACTERIZATION, AND ITS APPLICATIONS IN OLEDS, AND CORROSION PROTECTION

9.1 INTRODUCTION

In this chapter IX, the synthesis and characterization of a series of new complexes with metal ions Mn^{2+}, Co^{2+}, Ni^{2+}, Cu^{2+}, Zn^{2+}, Cd^{2+}, Mg^{2+}, Ca^{2+}, Sr^{2+}, and Ba^{2+}, with aminoguanidine -2-naphthoate was discussed in a 1:2:2 ratio. They were characterized by the physiochemical method and thermal analysis. Metal complexes are structurally characterized by the X-ray powder diffraction method. The metal complexes are found to be promising aspirants as phosphorescent materials for OLED applications. However, no report is available on the transition metal complex as a phosphor in light-emitting diodes because the challenging factor is to match its electronic structure. This chapter focused on metal complexes with electron-rich hetero atoms as a chelating ligand in shaping photophysical, photometric, and photochemical properties. Our perspective is organized into sections on synthesis, spectral, thermal, structural, and photometric characterization of the title compound. The metal oxides synthesized from complexes were characterized, and they are used for their anticorrosive properties, which were determined from EIS studies. This electrochemical study confirms the excellent protection of the metal substrate by forming a physical barrier.

9.2 EXPERIMENTAL

9.2.1. Synthesis of complexes

The aminoguanidine bicarbonate (0.36 g, 2 mmol) solution was prepared in double-distilled water (20 mL) with constant stirring for 2 hours at room temperature using a magnetic stirrer. In the solution, white crystalline crystals of 2-naphthoic acid (0.17 g, 1 mmol) were mixed slowly till it became a clear homogenous solution. To the ensuing

mixture, metal nitrate solution was added in 1molar concentration with constant stirring and kept in the water bath for 30 min. The resulting solution were refluxed for 6 hrs to obtain crystalline metal complexes which were illustrated in **Figure 9.1**.
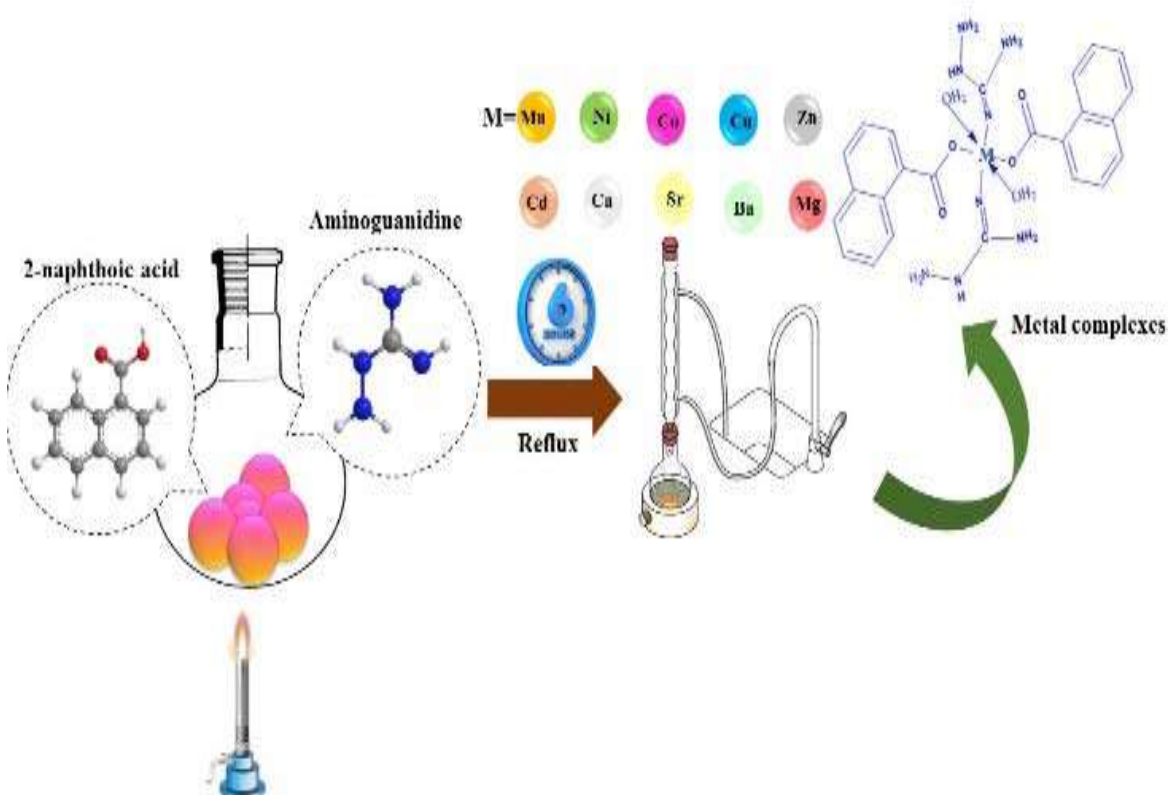
Figure 9.1 *Synthesis process.*

9.3 RESULTS AND DISCUSSION

9.3.1 Element analysis/ Analytical data

As from the preliminary observation, the metal complexes exhibit intense color differences and are soluble in the common organic solvent. The spectral and analytical data indicate the formation of the general formula, which is represented in **Tables 9.1** and **9.2.**

Table 9.1 Analytical data						
Metal Complexes	**Molecular weight (g/mol)**	**Color**	**pH**	**Melting point (oC)**	**Metal (%)**	
					Found	**Calc**
$[Mn(C_2H_8N_4O_3)_2 C_{10}H_7(2COO)\}_2.2H_2O]$	545.45	Light pink	7	225	10.07	10.03
$[Co(C_2H_8N_4O_3)_2 \{C_{10}H_7(2COO)\}_2.2H_2O]$	549.49	Pink	6	168	10.7	10.00
$[Ni(C_2H_8N_4O_3)_2 \{C_{10}H_7(2COO)\}_2.2H_2O]$	549.21	Green	7	165	10.6	10.05
$[Cu(C_2H_8N_4O_3)_2 \{C_{10}H_7(2COO)\}_2.2H_2O]$	554.06	Blue	8	176	11.4	11.3
$[Zn(C_2H_8N_4O_3)_2 \{C_{10}H_7(2COO)\}_2.2H_2O]$	555.89	white	8	195	11.7	11.6
$[Cd(C_2H_8N_4O_3)_2 \{C_{10}H_7(2COO)\}_2.2H_2O]$	602.93	white	7	213	18.6	18.5
$[Ca(C_2H_8N_4O_3)_2 \{C_{10}H_7(2COO)\}_2.2H_2O]$	530.59	White	7	269	17.5	17.6
$[Sr(C_2H_8N_4O_3)_2 \{C_{10}H_7(2COO)\}_2.2H_2O]$	578.13	White	6	242	15.1	15.2
$[Ba(C_2H_8N_4O_3)_2 \{C_{10}H_7(2COO)\}_2.2H_2O]$	627.84	White	6	213	21.8	21.7
$[Mg(C_2H_8N_4O_3)_2 \{C_{10}H_7(2COO)\}_2.2H_2O]$	514.82	White	6	245	14.7	14.8

| Table 9.2 Elemental data				
Complexes	% Carbon Found (Cald)	% Hydrogen Found (Cald)	% Nitrogen Found (Cald)	% Oxygen Found (Cald)
[Mn(C₂H₈N₄ O₃)₂ {C₁₀H₇(2COO)}₂.2H ₂O]	52.85 (52.80)	4.80 (4.79)	20.54 (20.53)	11.73 (11.72)
[Co(C₂H₈N₄ O₃)₂ {C₁₀H₇(2COO)}₂.2H ₂O]	52.46 (52.45)	4.77 (4.76)	20.39 (20.38)	11.65 (11.64)
[Ni(C₂H₈N₄ O₃)₂ {C₁₀H₇(2COO)}₂.2H ₂O]	52.49 (52.48)	4.77 (4.76)	20.40 (20.39)	11.65 (11.64)
[Cu(C₂H₈N₄ O₃)₂ {C₁₀H₇(2COO)}₂.2H ₂O]	52.03 (52.02)	4.73 (4.72)	20.22 (20.21)	11.55 (11.54)
[Zn(C₂H₈N₄ O₃)₂ {C₁₀H₇(2COO)}₂.2H ₂O]	51.85 (51.84)	4.71 (4.70)	20.16 (20.15)	11.51 (11.50)
[Cd(C₂H₈N₄ O₃)₂ {C₁₀H₇(2COO)}₂.2H ₂O]	47.81(47.80)	4.35 (4.30)	18.58 (18.56)	10.61 (10.60)
[Ca(C₂H₈N₄ O₃)₂ {C₁₀H₇(2COO)}₂.2H ₂O]	54.33 (54.32)	4.94 (4.93)	21.12 (21.10)	12.06 (12.05)
[Sr(C₂H₈N₄ O₃)₂ {C₁₀H₇(2COO)}₂.2H ₂O]	49.86 (49.85)	4.53 (4.52)	19.38 (19.37)	11.07 (11.06)
[Ba(C₂H₈N₄ O₃)₂ {C₁₀H₇(2COO)}₂.2H ₂O]	45.91(45.90)	4.17 (4.18)	17.85 (17.84)	10.19 (10.18)
[Mg(C₂H₈N₄ O₃)₂ {C₁₀H₇(2COO)}₂.2H ₂O]	55.99 (55.98)	5.09 (5.08)	21.77 (21.70)	12.43 (12.42)

9.3.2 FT-IR analysis

In the FT-IR spectra (**Figure 9.2)**, all the metal complexes with aromatic C-H stretching frequencies were observed around 3100-3000 cm^{-1}. Due to the existence of strong intermolecular H-bonding, their spectra display broadband due to the O-H stretching vibrations, in which the peak appears at 3589-3400 cm^{-1} and a strong band due to C=O

vibration, which is due to the intensity in the region at 1800-1695 cm^{-1}. The carboxylic acids of -COOH show a weak band in the region 685-489 cm^{-1} and the formation of π-π interaction between the C=O. Two bands of C-O and O-H stretching vibrations occur at 1215-1325 cm^{-1} and 1400-1445 cm^{-1}, respectively. C=N and N-N stretching frequencies of aminoguanidine occur at 1695 cm^{-1} and 1116 cm^{-1} which confirm the formation of metal complexes in **Table 9.3** [1].
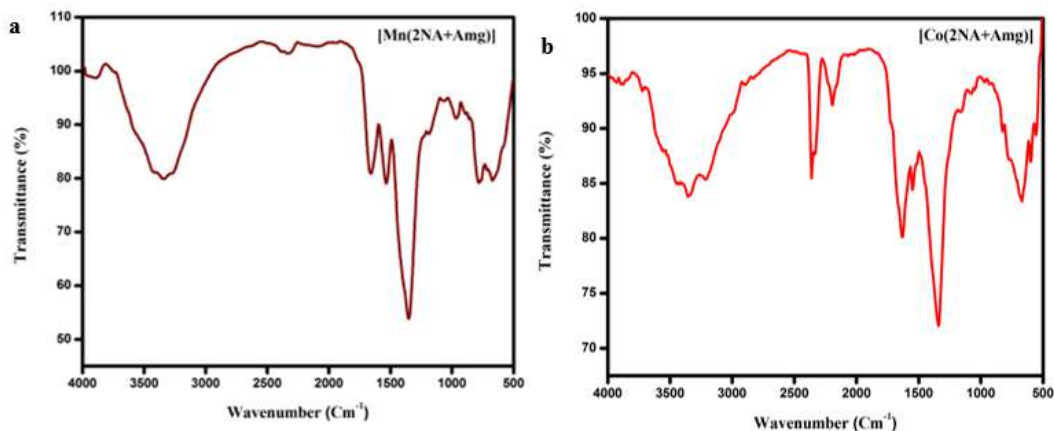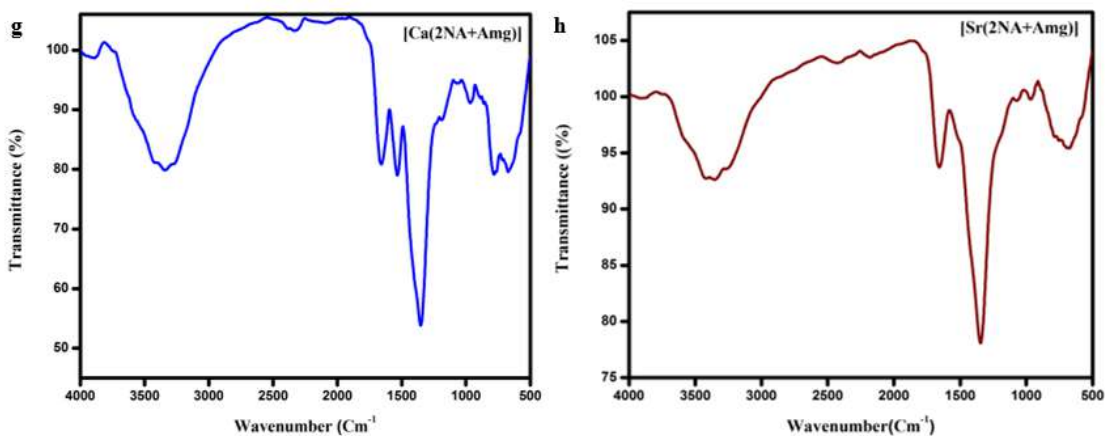

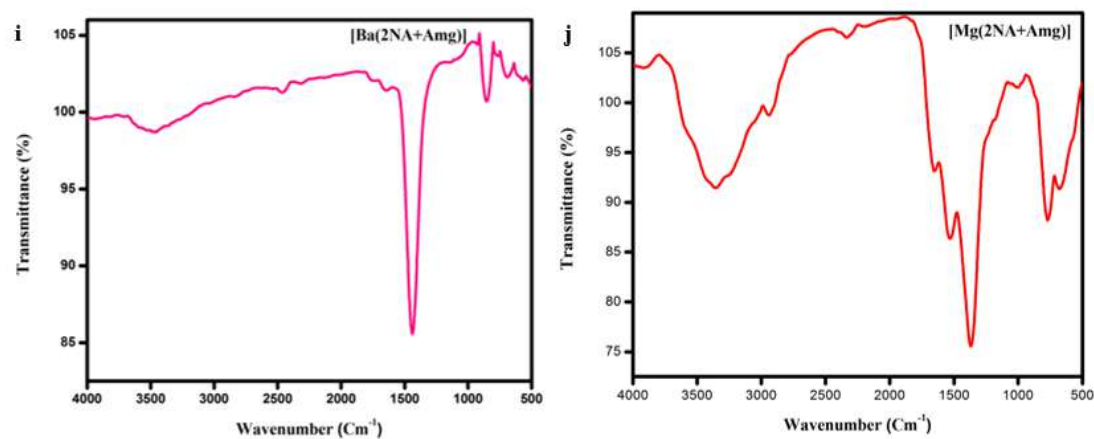**Figure 9.2** *FT-IR spectra of a)Mn(II) b)Co(II) complex*
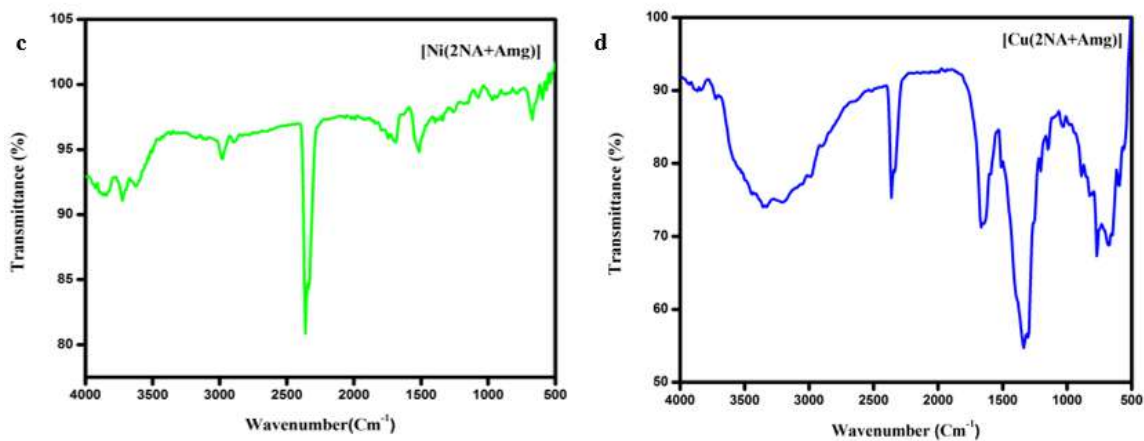
Figure 9.2 *FT-IR spectra of c)Ni(II) d)Cu(II) complex*
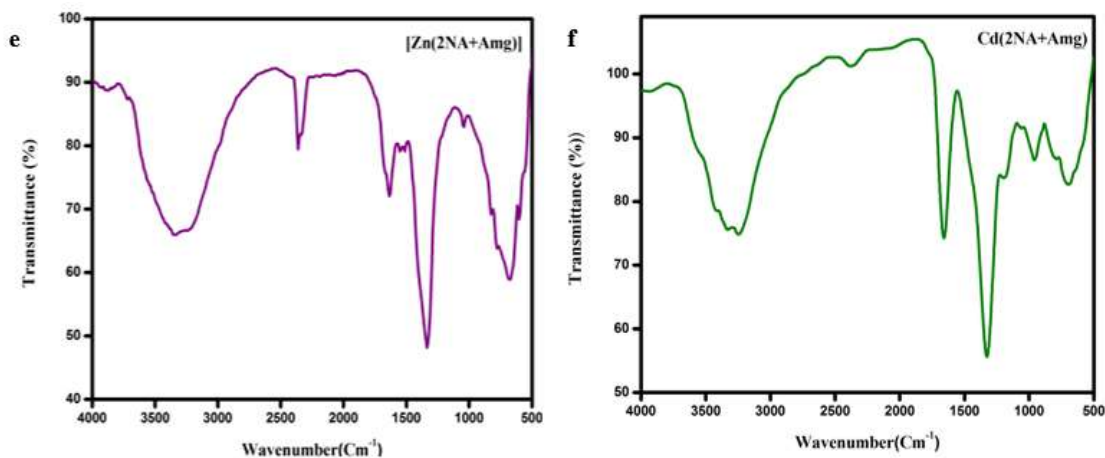
Figure 9.2 *FT-IR spectra of e) Zn (II) f)Cd(II) complex*

Figure 9.2 *FT-IR spectra of g)Ca(II) h)Sr(II) complex*

**Figure 9.2** *FT-IR spectra of i) Ba (II) j)Mn (II) complex*

<table>
<tr><th colspan="7">Table 9.3 IR Spectra.</th></tr>
<tr>
<th>Complexes</th>
<th>$\nu_{(OH)}$ cm^{-1}</th>
<th>ν_{asym} (C=O) cm^{-1}</th>
<th>ν_{sym} (C=O) cm^{-1}</th>
<th>$\upsilon_{(NH)}$ cm^{-1}</th>
<th>$\upsilon_{(N-N)}$ cm^{-1}</th>
<th>M-O cm^{-1}</th>
</tr>
<tr><td>[Mn(C$_2$H$_8$N$_4$ O$_3$)$_2$ {C$_{10}$H$_7$(2COO)}$_2$.2H $_2$O]</td><td>3036</td><td>1668</td><td>1531</td><td>3372</td><td>1098</td><td>499</td></tr>
<tr><td>[Co(C$_2$H$_8$N$_4$ O$_3$)$_2$ {C$_{10}$H$_7$(2COO)}$_2$.2H $_2$O]</td><td>3176</td><td>1673</td><td>1543</td><td>3343</td><td>1087</td><td>498</td></tr>
<tr><td>[Ni(C$_2$H$_8$N$_4$ O$_3$)$_2$ {C$_{10}$H$_7$(2COO)}$_2$.2H $_2$O]</td><td>3116</td><td>1667</td><td>1517</td><td>3657</td><td>1213</td><td>488</td></tr>
<tr><td>[Cu(C$_2$H$_8$N$_4$ O$_3$)$_2$ {C$_{10}$H$_7$(2COO)}$_2$.2H $_2$O]</td><td>3048</td><td>1662</td><td>1512</td><td>3361</td><td>1087</td><td>497</td></tr>
<tr><td>[Zn(C$_2$H$_8$N$_4$ O$_3$)$_2$ {C$_{10}$H$_7$(2COO)}$_2$.2H $_2$O]</td><td>3073</td><td>1668</td><td>1517</td><td>3321</td><td>1109</td><td>499</td></tr>
<tr><td>[Cd(C$_2$H$_8$N$_4$ O$_3$)$_2$ {C$_{10}$H$_7$(2COO)}$_2$.2H $_2$O]</td><td>3035</td><td>1658</td><td>1515</td><td>3342</td><td>1110</td><td>488</td></tr>
<tr><td>[Ca(C$_2$H$_8$N$_4$ O$_3$)$_2$ {C$_{10}$H$_7$(2COO)}$_2$.2H $_2$O]</td><td>3132</td><td>1647</td><td>1511</td><td>3353</td><td>1332</td><td>462</td></tr>
<tr><td>[Sr(C$_2$H$_8$N$_4$ O$_3$)$_2$ {C$_{10}$H$_7$(2COO)}$_2$.2H $_2$O]</td><td>3192</td><td>1619</td><td>1558</td><td>3374</td><td>1382</td><td>491</td></tr>
<tr><td>[Ba(C$_2$H$_8$N$_4$ O$_3$)$_2$ {C$_{10}$H$_7$(2COO)}$_2$.2H $_2$O]</td><td>3241</td><td>1639</td><td>1528</td><td>3423</td><td>1352</td><td>498</td></tr>
<tr><td>[Mg(C$_2$H$_8$N$_4$ O$_3$)$_2$ {C$_{10}$H$_7$(2COO)}$_2$.2H $_2$O]</td><td>3320</td><td>1639</td><td>1481</td><td>3877</td><td>1019</td><td>485</td></tr>
</table>

9.3.3 Electronic spectra

The metal complexes exhibit a band around 240-340 nm attributable to the transition of the aromatic ring, which exhibits the π-π*, and n- π* transition. The complex band was shifted to the longer wavelength towards the metal ions, and it confirms the formation of metal complexes which is examined in **Figure 9.3 (a-j).** The direct band gap for all the metal complexes found under optimal conditions was calculated from the

equation, which is already explained in Chapter VII, where semiconductor materials exhibit the region where light absorption increases steeply and linearly as energy increases. The band gap energy is estimated at the x-axis intersection point of the Tauc plot's linear fit. The value of the band gap energy (Eg) from 3.6 -4.7 eV is exhibited in **Figure 9.3(a'-b')**.
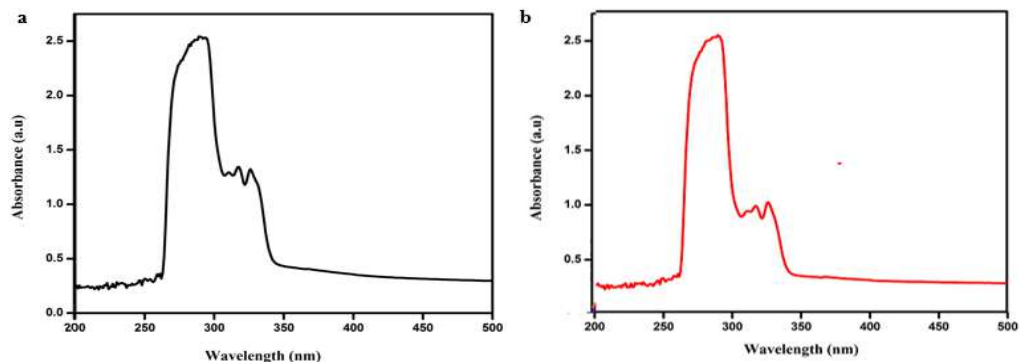
Figure 9.3 *UV-visible spectra of a) Mn (II) b) Co (II) complex*
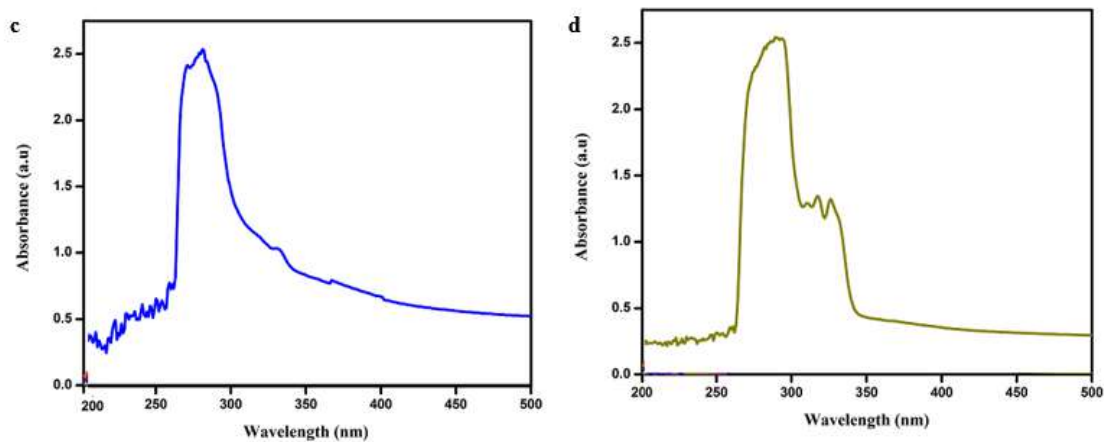
Figure 9.3 *UV-visible spectra of c) Ni (II) d) Cu (II) complex*

209
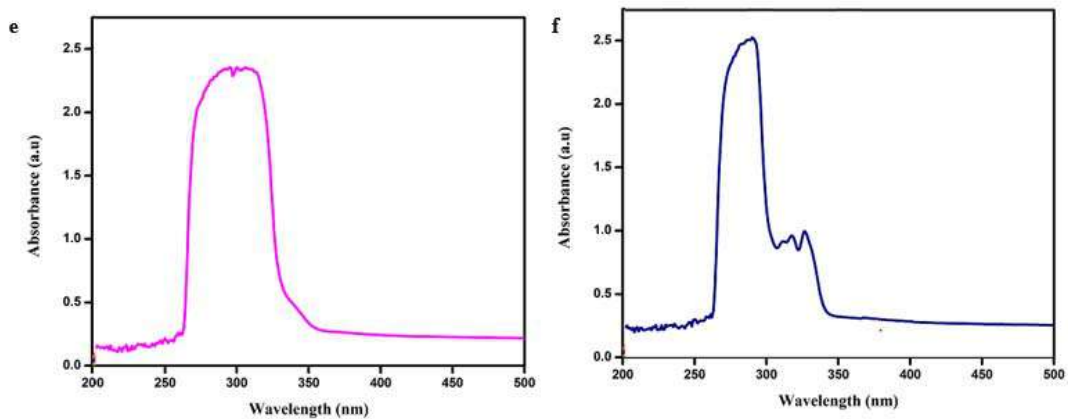
Figure 9.3 *UV-visible spectra of e) Zn (II) f) Cd (II) complex*

Figure 9.3 *UV-visible spectra of g) Ca (II) h) Sr (II) complex*

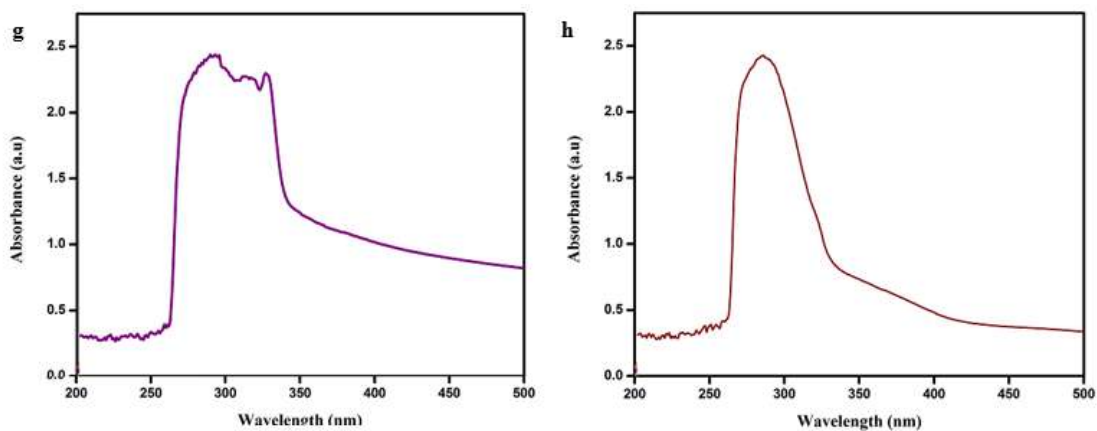**Figure 9.3** *UV-visible spectra of i) Ba (II) j) Mg (II) complex*

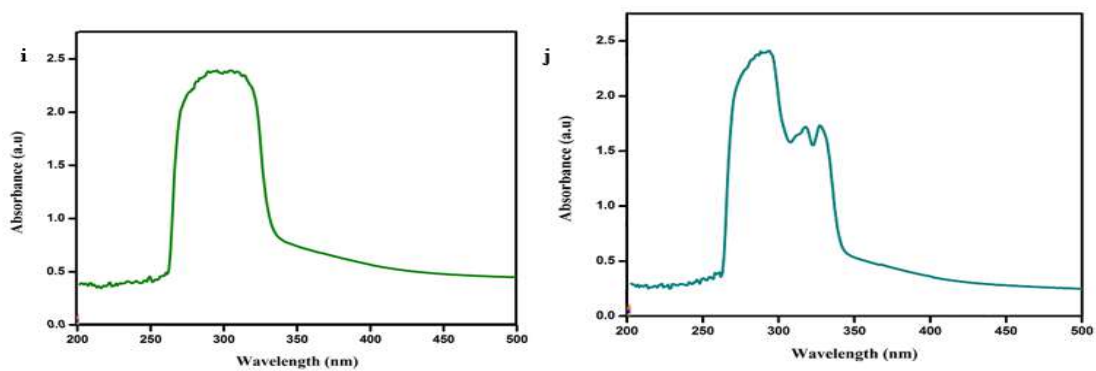**Figure 7.3** *UV-visible spectra of a') Mn (II) b') Co (II) complex*

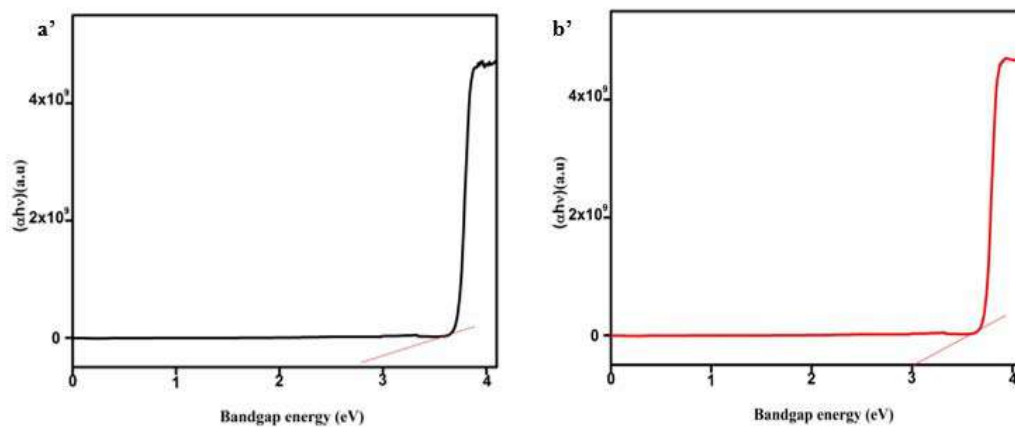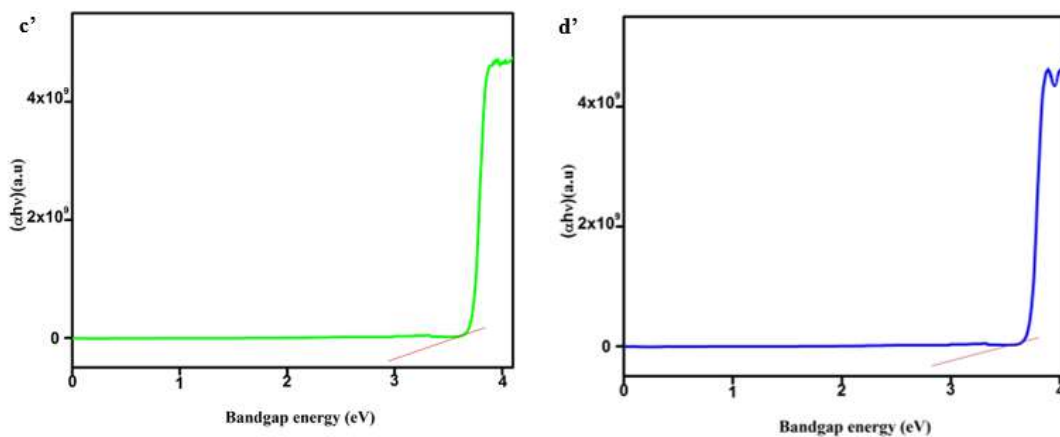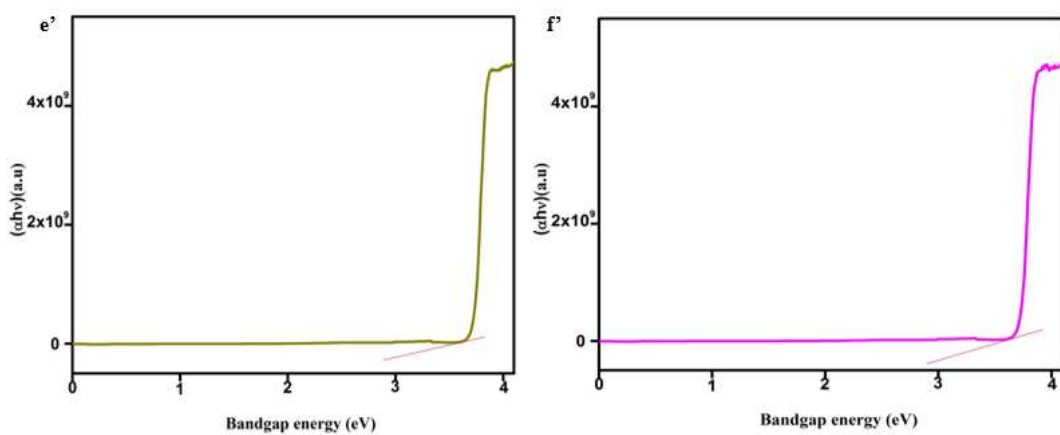**Figure 7.3** *UV-visible spectra of c') Ni (II) d') Cu (II) complex*

Figure 7.3 *UV-visible spectra of e') Zn (II) f') Cd (II) complex*

211
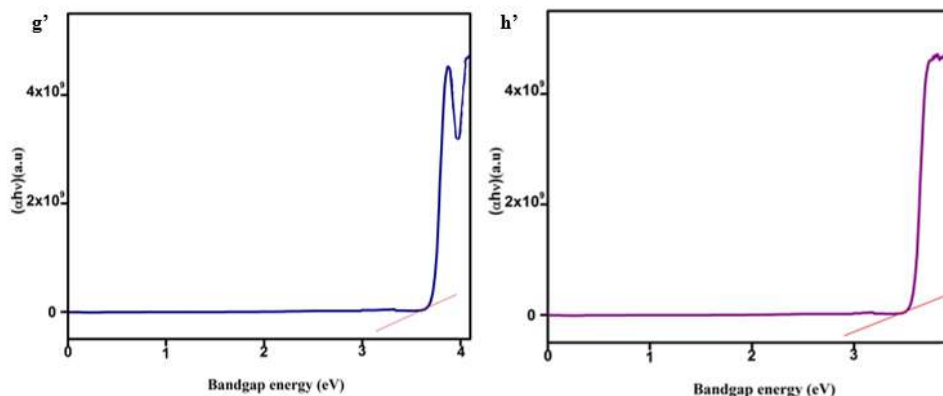
Figure 7.3 *UV-visible spectra of g') Ca (II) h') Sr (II) complex*
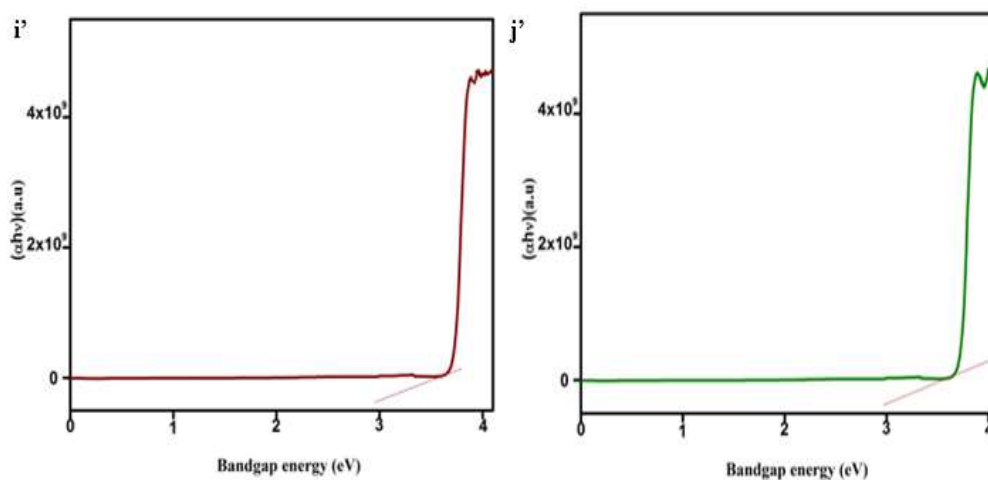
Figure 7.3 *UV-visible spectra of i') Ba (II) j') Mg (II) complex*

9.3.4 Thermogravimetry Differential Thermal Analysis(TG-DTA)

The TG-DTA of all the metal complexes was carried out in an nitogen atmosphere at a heating frequency of 10°C per minute from ambient conditions to 800°C. They decomposed in two to three steps, as illustrated in **Figure 9.4,** leaving metal oxide as a final residue. From the TG curves, it is detected that the first step resembles a loss of water molecules, and the temperature occurred from 210°C -380°C. The subsequent phases display the decomposition of organic molecules and exhibit a temperature of 380-554 °C, respectively. The schematic decomposition is represented below and illustrated in **Table 9.4**.

Thermal decomposition scheme (1)

$[M(C_2H_8N_4O_3)_2\{C_{10}H_7(2COO)\}\ 2H_2O]\ \xrightarrow{100\text{-}210\ ^0C}\ [M(C_2H_8N_4O_3)_2\{C_{10}H_7(2COO)\}_2\ ]$ - $2H_2O$

$[M(C_2H_8N_4O_3)_2\{C_{10}H_7(2COO)\}_2]\ \xrightarrow{210\text{-}3380^\circ C}\ [M\{C_{10}H_7(2COO)\}_2]$ - $C_2H_8N_4O_3$

$[M\{C_{10}H_7(2COO)\}_2]\ \xrightarrow{380\text{-}600^\circ\ C}\ [MO]$
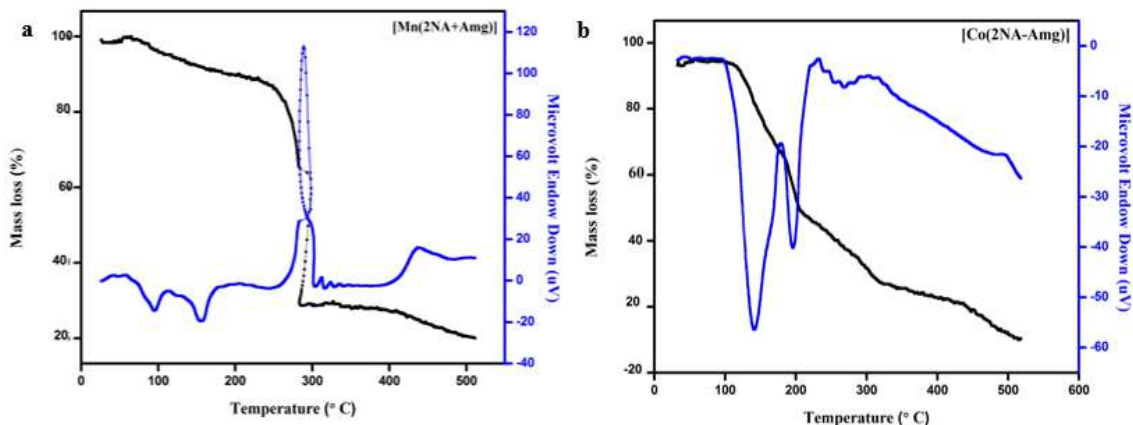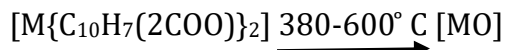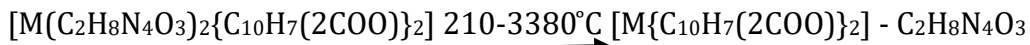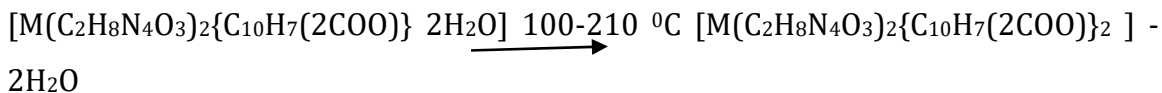
Figure 9.4 *TG-DTA curve of a) Mn(II) b) Co(II) complex*
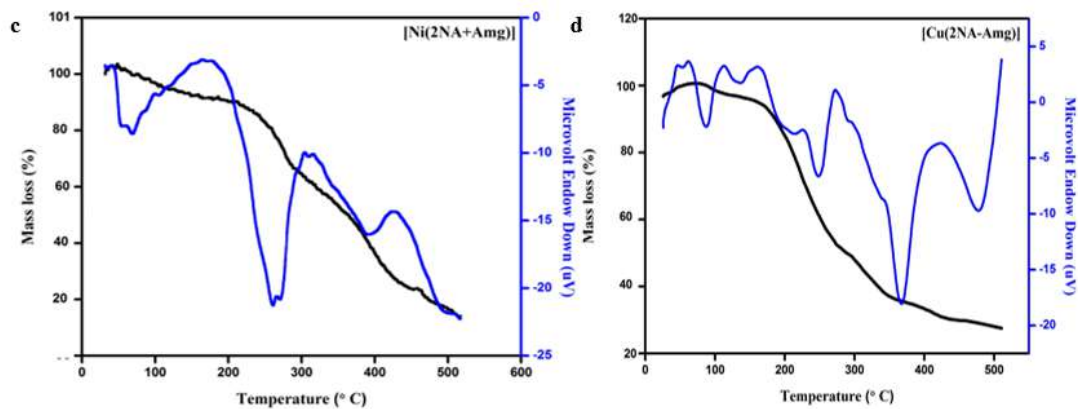
Figure 9.4 *TG-DTA curve of c) Ni (II) d) Cu (II) complex*
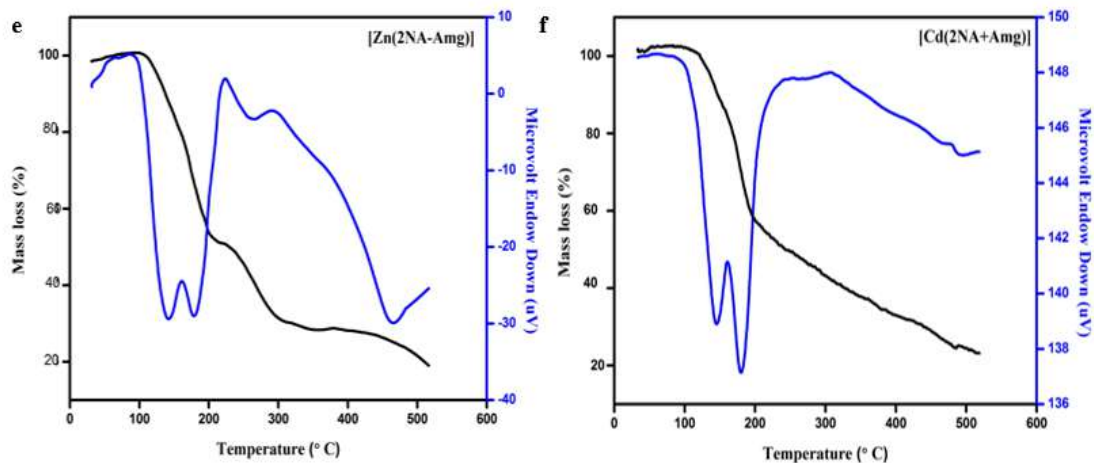
Figure 9.4 *TG-DTA curve of e) Zn (II) f) Cd (II) complex*
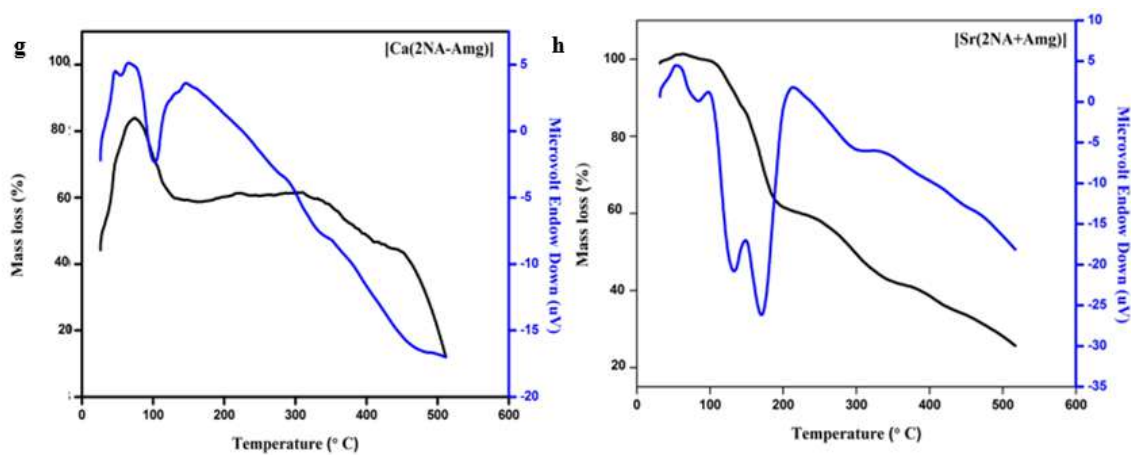
Figure 9.4 *TG-DTA curve of g) Ca(II) h) Sr (II) complex*
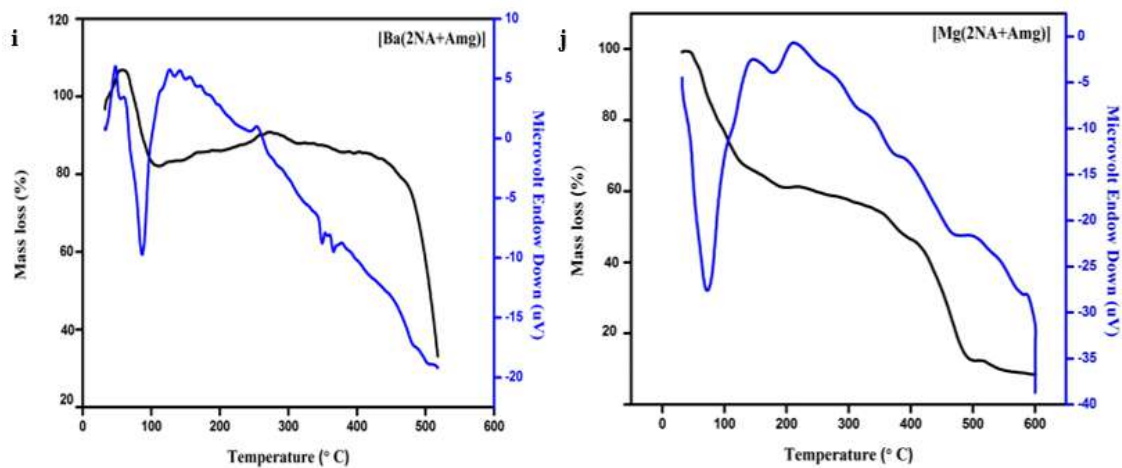
Figure 9.4 *TG-DTA curve of i) Ba (II) j) Mg (II) complex*

9.3.5 Powder-XRD

The P-XRD patterns for all the metal coordination complexes were recorded (2 hours 0-80° C), which are observed in **Figure 9.5**. It indicates that the sharp crystalline peak signifies their crystalline phase. The particle size (d $_{XRD}$) of the complexes was calculated by Scherer's formula **(Eq 9.1)**. The crystalline size occurs around 20-80 nm. The observed XRD peak is illustrated in **Table 9.5**.

$$D = \frac{k\lambda}{B_{hkl}\, Cos\, \theta_{hkl}}$$ **Eq 9.1**

Figure 9.5 *XRD peak of a) Mn II) b) Co (II) complex*

Figure 9.5 *XRD peak of c) Ni (II) d) Cu (II) complex*

Figure 9.5 *XRD peak of e) Zn (II) f) Cd (II) complex*

Figure 9.5 *XRD peak of g) Ca (II) h) Sr (II) complex*
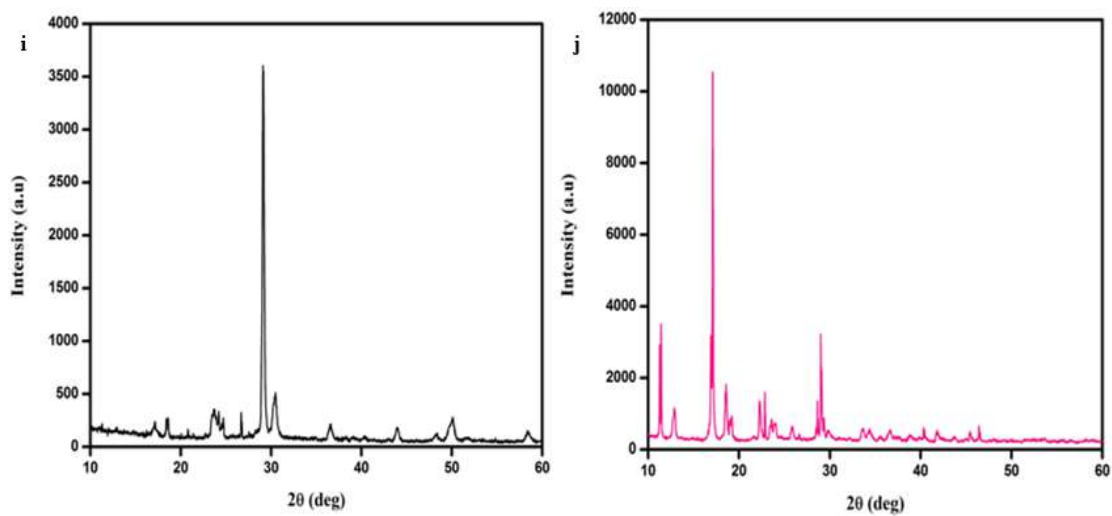
Figure 9.5 *XRD peak of i) Ba (II) j) Mg (II) complex*

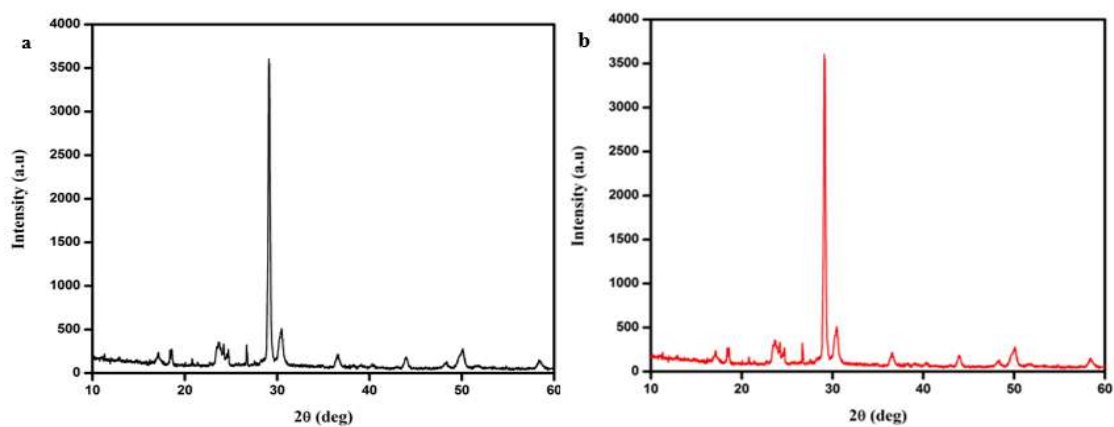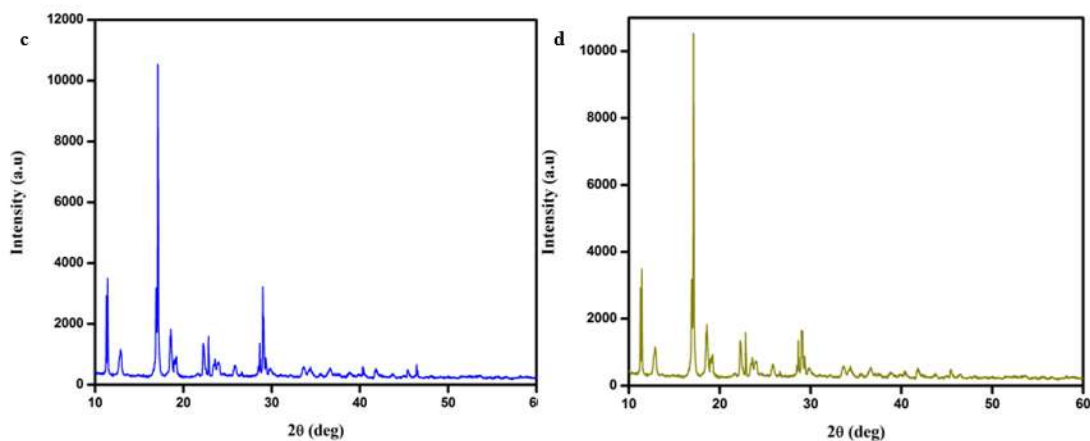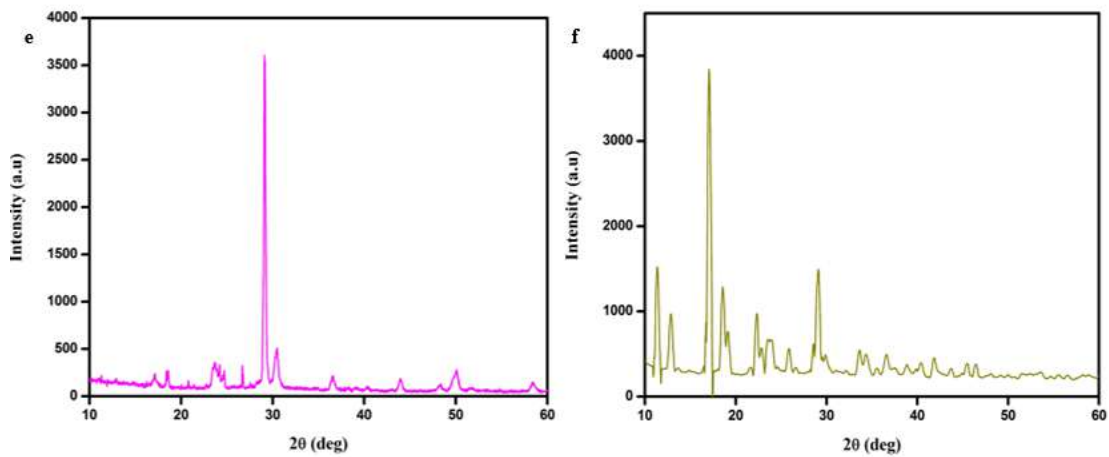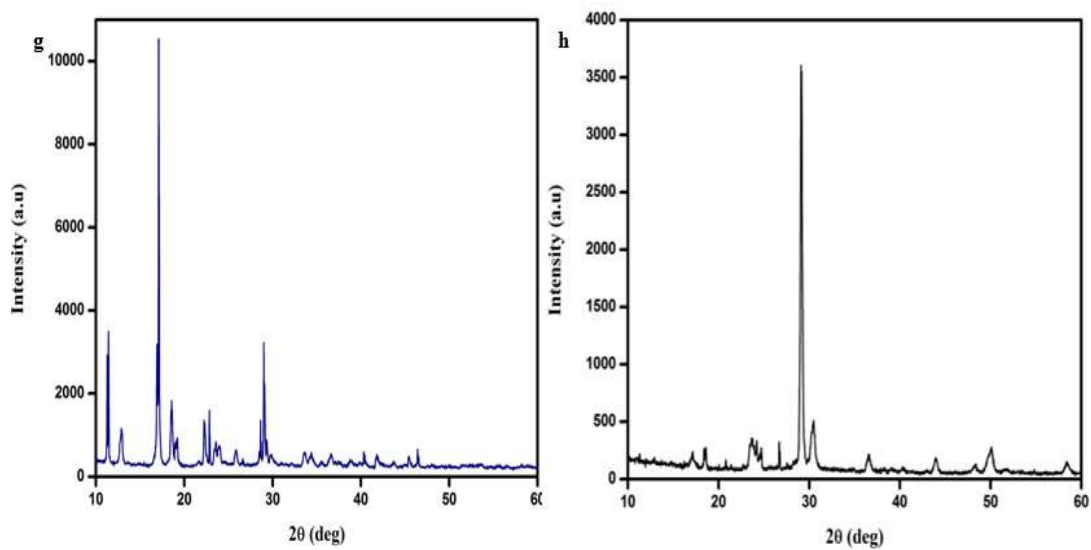|		Thermogravimetry			
Metal complexes	**DTA peak**	**Temp Range(°C)**	**Weight loss (%)**		**Decomposition Nature of the compound**
			Obsd.	**Calcd.**	
$[Mn(C_2H_8N_4O_3)_2\{C_{10}H_7(2COO)\}_2.2H_2O]$	(+) 110,(+) 298	55-350	80	90	Dehydration and partial decomposition
	(-) 425	350-700	100	100	Complete decomposition to MnO_2
$[Co(C_2H_8N_4O_3)_2\{C_{10}H_7(2COO)\}_2.2H_2O]$	(+) 150, (+) 199	100-320	90	90	Loss of water molecules
	(-) 250, (-) 300	360-600	100	100	Completely decomposition CO_3O_4
$[Ni(C_2H_8N_4O_3)_2\{C_{10}H_7(2COO)\}_2.2H_2O]$	(+) 285	55-250	80	90	Decomposition
	(-) 315,(-) 425	260-500	100	100	Complete decomposition to NiO
$[Cu(C_2H_8N_4O_3)_2\{C_{10}H_7(2COO)\}_2.2H_2O]$	(+) 210, (+) 215	100-250	90	90	Decomposition
	(-) 350, (-) 490, (-) 450	260-600	100	100	Complete formation of CuO
$[Cd(C_2H_8N_4O_3)_2\{C_{10}H_7(2COO)\}_2.2H_2O]$	(+) 199, (+) 319	100-400	70	80	Partial decomposition
	(-) 300, (-) 345	410-500	100	100	Formation of CdO
$[Zn(C_2H_8N_4O_3)_2\{C_{10}H7(1COO)\}_2.2H_2O]$	(+) 175	55-300	80	90	Dehydration
	(-) 298	320-500	100	100	ZnO formation
$[Ca(C_2H_8N_4O_3)_2\{C_{10}H_7(2COO)\}_2.2H_2O]$	(+) 110, (+) 200	100-400	90	100	Dehydration
	(-) 210, (-) 425	420-700	100	100	Complete decomposition to CaO
$[Sr(C_2H_8N_4O_3)_2\{C_{10}H_7(2COO)\}_2.2H_2O]$	(+) 195, (+) 295	100-400	90	90	Dehydration
	(-) 299, (-) 325	425-600	100	100	Complete decomposition to SrO
$[Ba(C_2H_8N_4O_3)_2\{C_{10}H_7(2COO)\}_2.2H_2O]$	(+) 74, (+) 160	55-166	85	90	Melting
	(-) 299, (-) 425	166-600	100	100	Complete decomposition to BaO
$[Mg(C_2H_8N_4O_3)_2\{C_{10}H_7(2COO)\}_2.2H_2O]$	(+) 190	55-200	80	80	Loss of water molecules
	(-) 265, (-) 589	250-600	100	100	Complete decomposition to MgO

Table 9.4 *Thermal Analysis*

Table 9.5 *P-XRD pattern for metal complexes*							
Complex	2θ	FWHM B_{size} (°)	D(space)	Complex	2θ	FWHM B_{size} (°)	D(space)
[Mn(C$_2$H$_8$N$_4$O$_3$)$_2$ {C$_{10}$H$_7$(2COO)}$_2$.2H$_2$O]	13.12	0.461	18.13	[Cd(C$_2$H$_8$N$_4$O$_3$)$_2$ {C$_{10}$H$_7$(2COO)}$_2$.2H$_2$O]	13.13	0.461	18.13
	16.1	0.469	17.88		16.02	0.469	17.88
	19.3	0.463	18.19		19.31	0.463	18.19
	21.87	0.502	16.85		21.88	0.502	16.85
	27.64	0.565	15.14		27.63	0.565	15.13
	29.7	0.596	14.41		29.71	0.596	14.41
[Co(C$_2$H$_8$N$_4$O$_3$)$_2$ {C$_{10}$H$_7$(2COO)}$_2$.2H$_2$O]	13.53	0.461	18.14	[Ca(C$_2$H$_8$N$_4$O$_3$)$_2$ {C$_{10}$H$_7$(2COO)}$_2$.2H$_2$O]	13	0.461	18.13
	17.14	0.469	17.91		17.01	0.469	17.90
	19.09	0.463	18.19		18	0.463	18.16
	22.6	0.502	16.87		21	0.502	16.82
	27.75	0.565	15.14		26	0.565	15.08
	31.35	0.596	14.47		31.1	0.596	14.46
[Ni(C$_2$H$_8$N$_4$O$_3$)$_2$ {C$_{10}$H$_7$(2COO)}$_2$.2H$_2$O]	12.4	0.461	18.12	[Sr(C$_2$H$_8$N$_4$O$_3$)$_2$ {C$_{10}$H$_7$(2COO)}$_2$.2H$_2$O]	12.54	0.461	18.12
	16.21	0.469	17.88		16.25	0.469	17.88
	19.09	0.463	18.19		19.2	0.463	18.19
	23.41	0.502	16.89		23.4	0.502	16.89
	24.97	0.565	15.05		24.9	0.565	15.05
	27.75	0.596	14.35		27.7	0.596	14.35
[Cu(C$_2$H$_8$N$_4$O$_3$)$_2$ {C$_{10}$H$_7$(2COO)}$_2$.2H$_2$O]	13.12	0.461	18.13	[Ba(C$_2$H$_8$N$_4$O$_3$)$_2$ {C$_{10}$H$_7$(2COO)}$_2$.2H$_2$O]	13.25	0.461	18.13
	19.3	0.469	17.96		19.35	0.469	17.96
	21.57	0.463	18.26		21.6	0.463	18.26
	27.02	0.502	17.01		27.19	0.502	17.02
	29.29	0.565	15.19		29.3	0.565	15.19
	32.16	0.596	14.50		32.2	0.596	14.50
[Zn(C$_2$H$_8$N$_4$O$_3$)$_2$ {C$_{10}$H$_7$(2COO)}$_2$.2H$_2$O]	12.4	0.461	18.12	[Mg(C$_2$H$_8$N$_4$O$_3$)$_2$ {C$_{10}$H$_7$(2COO)}$_2$.2H$_2$O]	12.39	0.461	18.12
	16.52	0.469	17.89		15.62	0.469	17.87
	19.09	0.463	18.19		19.05	0.463	18.19
	24.76	0.502	16.94		25.76	0.502	16.97
	26.19	0.565	15.09		27.2	0.565	15.12
	27.84	0.596	14.35		28.85	0.596	14.39

9.3.6 Antimicrobial activity towards metal complexes

The antibacterial efficiency of the metal complexes against Ni (II), Co (II), Cu (II), and Zn (II) was investigated using the disc diffusion method. *Escherichia coli* and *Staphylococcus aureus* were the targets of antibacterial experiments. The antibacterial activity against *Staphylococcus aureus* and *Escherichia coli* is indicated in **Table 9.6** and **Figure 9.6, 9.7**. Zn (II) exhibits the highest levels of inhibition (14 mm and 16 mm, respectively) against *Staphylococcus aureus* and *Escherichia coli* among the produced metal complexes. The heteroatom in metal ions suggests a greater tendency towards a biomolecular interaction. The polarity change in metal complexes might be the cause of improved antimicrobial activity.
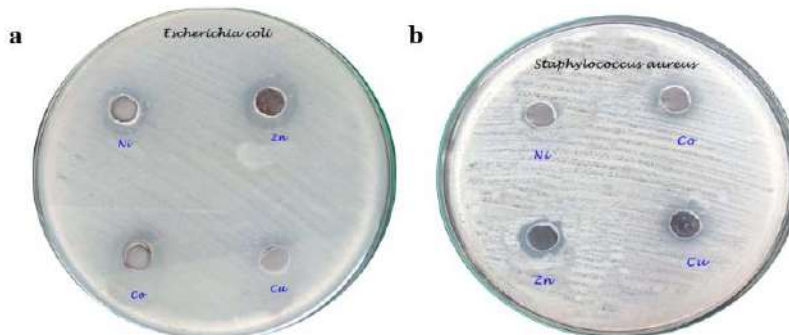
Figure 9.6 *Antimicrobial activity of the complex against a) Staphylococcus aureus b) Escherichia coli*
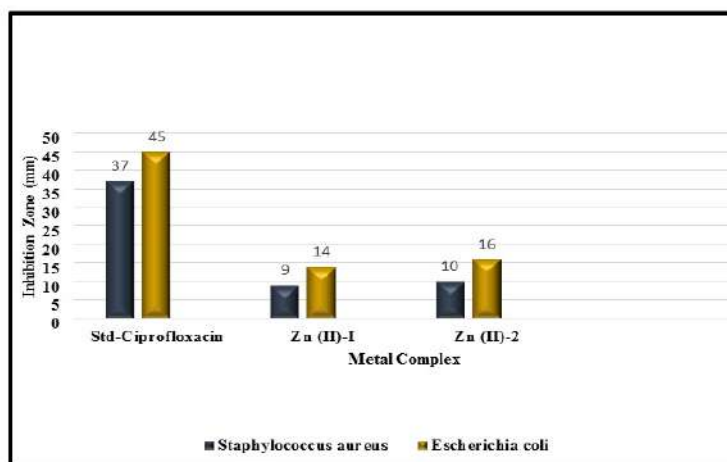
Figure 9.7 *Inhibition evaluation of the Zn (II) complex against bacteria*

Table 9.6 *Antibacterial Activity*		
	Inhibition zone (mm) (100µg/disc)	
Compound	*Staphylococcus aureus*	*Escherichia coli*
Standard – Ciprofloxacin	37	45
Zn(II)-1	9	14
Zn (II)-2	10	16

9.4 METAL COMPLEXES OF Ni (II), Co (II), AND Cu (II) FOR OLED's APPLICATIONS

9.4.1 Photoluminescence spectra

9.4.1.1 Photoluminescence spectra of Ni (II) complex

Emission spectra of the Ni (II) complex show excitation at 305 nm and three robust, broad bands at 343, 621, and 710 nm. The d^8 system of Ni^{2+} ions can occur both in tetrahedral and octahedral geometry. But the attained energy levels are allocated to distorted octahedral geometry and assigned as $A_{2g}(F) \rightarrow T_{2g}(F)$, $A_{2g}(F) \rightarrow T_{1g}(F)$ & $A_{2g}(F) \rightarrow T_{1g}(P)$. In addition, spin-allowed transitions (3) and spin-forbidden transitions (1) were observed. The luminescence properties of Ni (II) exist in two segments, namely green and red, which are designated to the $T_{2g}(D) \rightarrow A_{2g}(F)$ & $T_{2g}(D) \rightarrow T_{2g}(F)$ transitions.

9.4.1.2 Photoluminescence spectra of Co (II) complex

The band of cobalt emission occurs around 600–700 nm, allocated to $^2E(2G) \rightarrow {}^4A_2(4F)$ of the octahedral environment. The Co (II) complex displays an excitation peak at 309 nm associated with three strong, broad bands at 355 nm, 621 nm & 710 nm. The existing peak confirms the bivalency state of cobalt ions in an octahedral environment. For Co^{2+} ions in the ground state, 4F splits into $^4T_1$, $^4T_2$, and $^4A_2$ states, with the $^4T_1$ state being the lowest one.

In addition to that, it exhibits two emission bands in the visible region, which were assigned to $^4T_1(4P) \rightarrow ^4A_2(4F)$ and ^{4T1} (4P) $\rightarrow ^4T_2(4F)$ octahedral. Compared with other complexes, the cobalt moiety shows enhanced emission spectra, which may be recognized in the MLCT process (metal-to-ligand charge transfer). It offers excellent coordination abilities for complex [2].

9.4.1.3 Photoluminescence spectra of Cu (II) complex

For the Cu (II) complex, emission spectra show an excitation peak at 323 nm with three strong emission bands ranging from 355 to 800 nm; the primary emission peak is detected at 354 nm and the other at 620 nm & 739 nm. In agreement with crystal field theory, the d^9, Cu^{2+} ion splits into E_g and T_{2g}, with E_g being the ground state.

The Photoluminescence spectra for all metal complexes are revealed in **Figure 9.8a**. The diffuse reflectance spectra of synthesized compounds' samples were collected to measure the optical band gap energy (E_g). The optical band gap energy was evaluated as the connection point between the energy axis and the extrapolated line from the straight line of the absorption edge in a plot of Kubelkas Munk function vs. energy. The band gap values for emission spectra are observed at 2.84 eV, 2.86 eV, and 2.87 eV, respectively, as shown in **Figure 9.8 b**. The emission spectra inferred that the photoluminescence was directly associated with band gap energy. The band structure illustration as attained through the DFT scaffold is shown in **Figure 9.8c**.

222
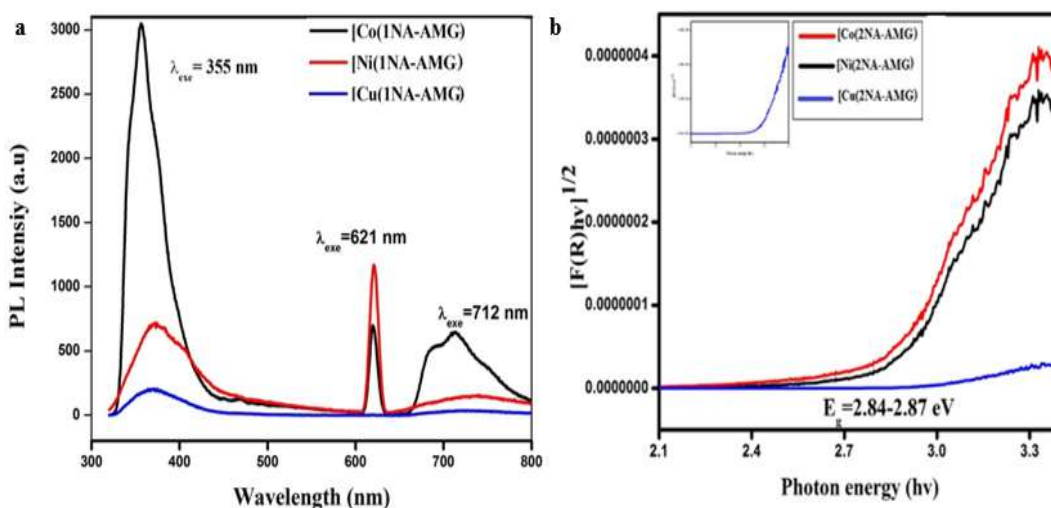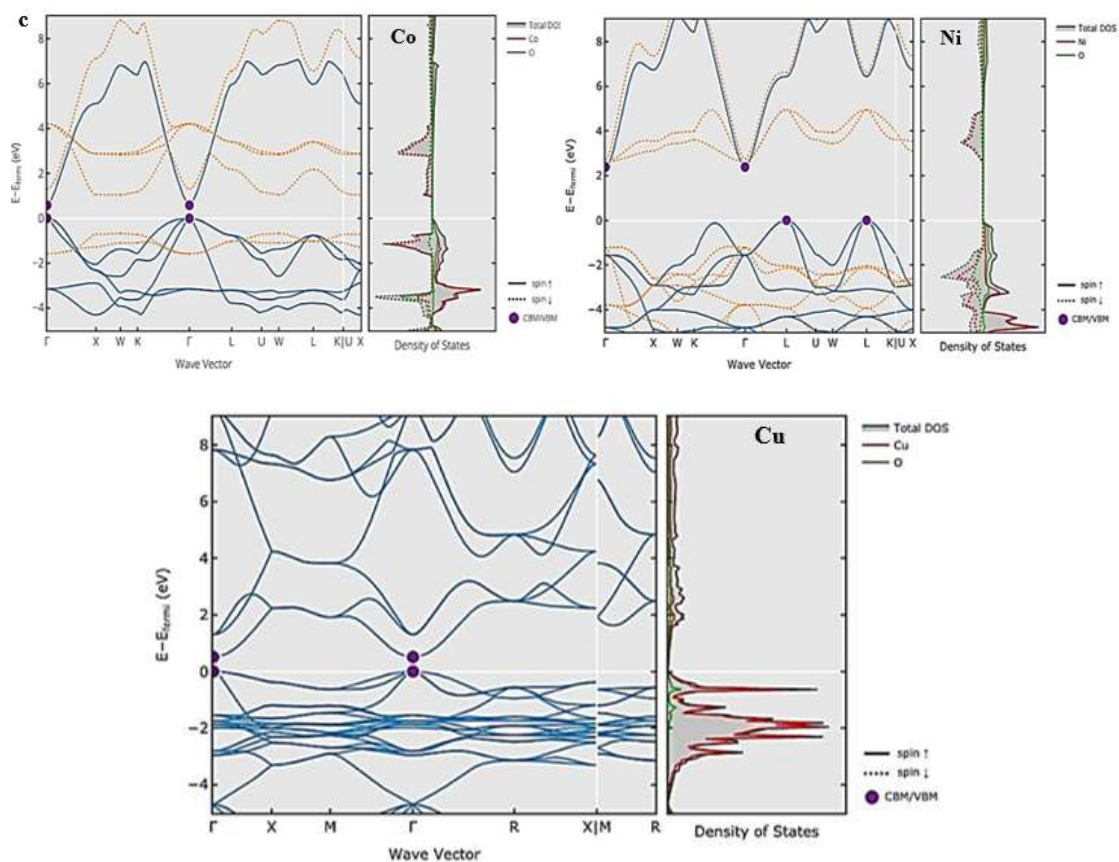
Figure 9.8 *a) Photoluminescence of metal complexes b) Energy band gap spectra*

c) Band structure from the DFT framework

9.4.1.4 Jablonski Energy Level

Jablonski represents the energy level within a molecule where the valency electron can be excited. The absorption of a photon from a particular energy level in the molecule results in the migration of electrons from the lower energy, ground state S_0 state, to the higher energy, excitation state S_1, which is indicated by the violet arrow in **Figure 9.9**. The light green arrow lying between the electronic states represents the migration of electrons that lose their absorbed energy from the higher energy state to the lower energy state by emitting photons. The fluorescence process occurs from 10^{-9} to 10^{-7} seconds, most frequently between the first excitation electron state and the ground state. The electronic state of F in the ground is represented by $A_{2g} + T_{1g} + T_{2g}$, D indicates $E_g + T_{2g}$, and P represents T_{1g}.
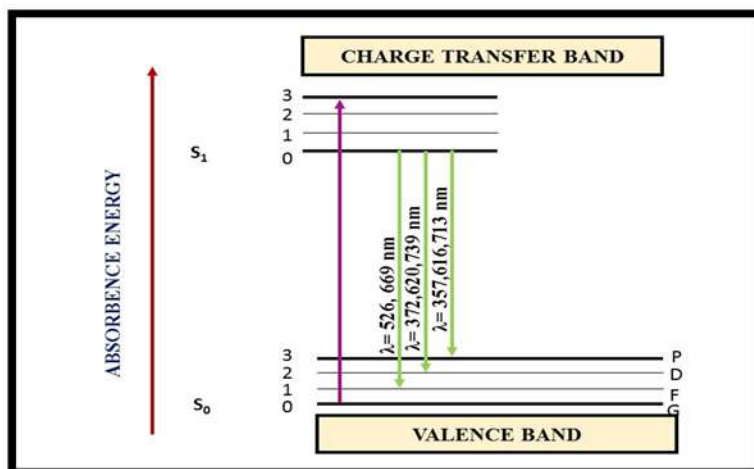
Figure 9.9 *Proposed Jablonski diagram*

9.4.2 Decay curve

Luminescence decay curves were attained at room temperature by scrutinizing all metal complexes' transition states (621 nm) and are represented in **Figure 9.10**. The photoluminescence decay curves show a good fit with only one exponential, and for [Ni(1NA-AMG-2 H_2O] at $A_{2g}(F) \rightarrow T_{2g}(F)$, [Co(1NA-AMG-2 H_2O] at $T_1(4P) \rightarrow A_2(4F)$ and [Cu(1NA-AMG-2 H_2O] display $3d^9 4s^1 \rightarrow 3d^{10}$ triplet transitions in the discharge (emission) spectrum. After 500nm, the intensity of the peak was lowered, which may be due to concentration quenching -transfer of energy from radiative to non-radiative ions. The decay lifetime was found to be 409 to 525 µs, respectively, and the results infer that all complexes have a good promising luminescence character for LED applications.
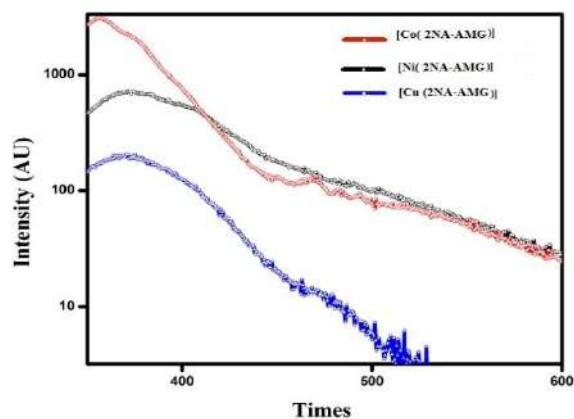
Figure 9.10 *PL decay spectrum for metal complexes*

9.4.3 Photometric properties

9.4.3.1 Chromaticity

The fundamental physical property of all light sources is the spectral power of light at all wavelengths. Chromaticity coordinates are evaluated from the spectral power distribution (SPD) and plotted as a two-dimensional graph to deliver the color communication of the given light source. Each color represents the suitable and distinctive diagram's point, whose positional variables are parallel to chromaticity coordinates. The CIE 1931 chromaticity X, Y coordinates (x, y) are evaluated from luminescence emission spectral data with the help of color-matching methods. The color of the light discharged from the source is denoted by the (x, y) coordinate revealed on a chromaticity diagram **(Figure 9.11)**. From this diagram, one can illustrate the influence of ions on the color of the emitted light. The line is stretched from blue to green, and the coordinates (color) position is denoted by a solid circle in the CIE diagram. CIE chromaticity coordinates of the test molecules and their values are presented in **Figure 9.11b** and **Table 9.7**. The observed CIE values range from X= 0.33 to 0.44, Y= 0.34 to 0.40. These results clearly showed the luminescence properties of synthesized complexes and had great hope as a white phosphor in OLED applications. It is evident from the values that the Cu ion emits in the blue region, and a digital photograph is placed inside **Figure 9.11a,** which also reveals blue emission.
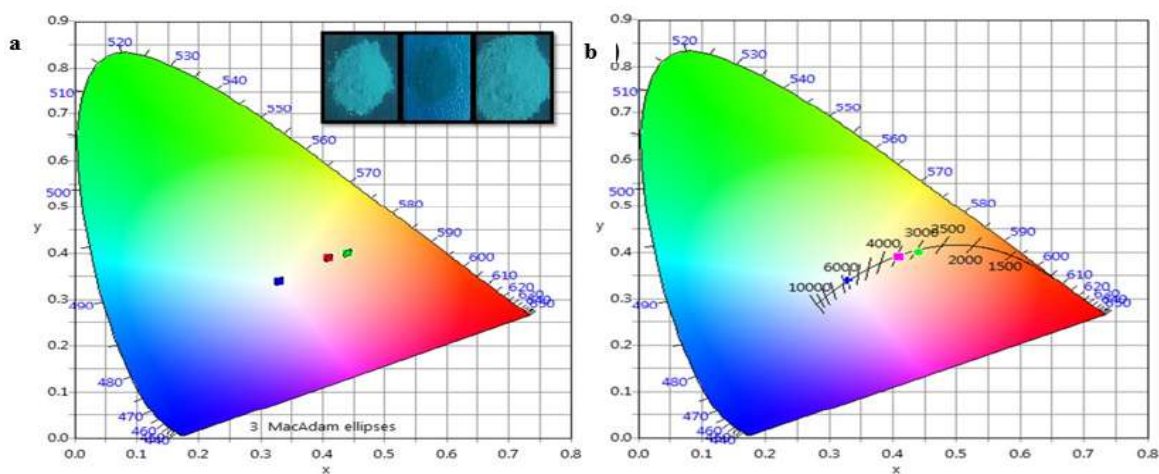
Figure 9.11 *a) The color of the emitted light b) CIE chromaticity coordinates*

Table 9.7 CRI values and coordinates for test sources				
Samples	**x**	**y**	**CRI(%)**	**Color**
[Co(2NA-AMG)]	0.41	0.39	15	Between warm white and neutral white
[Ni(2NA-AMG)]	0.44	0.40	10	Warm White
[Cu(2NA-AMG)]	0.33	0.34	90	Between daylight and sunlight

9.4.3.2 Color Temperature (CCT) and Duv

The correlated color temperature (CCT) describes the color manifestation of the emitted radiation, relating the original color to the color of a reference source, while warmth is up to a specific temperature. CCT was determined using the Planckian locus **(Figure 9.12a)** and was able to find out the nature of the source (warm or cool). The CCT rating for Ni (II) ion is below 3200 K, which implies a Planckian black-body source, and for Cu(II), it is 5278 K, a daylight source, and Co(II) at 3312 K as a mixed illuminant. From the CCT value (Table 4), copper and cobalt complexes are considered cool light sources, and nickel is warm light emitting source [3].

The Duv (Delta u, v) distance metric indicates the relative distance to the black body. Both CCT value and Duv are generally used to connect the emitted light's color and describe the chromaticity. If the chosen source lies below the black-body locus, the Duv value is negative, and if it lies above the black-body locus, the value becomes positive. The Duv metric is evaluated with the help of CIE 1931 XY values using the subsequent formula **Eq. (9.2)**,

$$v = \frac{4x}{-2x + 2y + 3}$$

$$v = \frac{6x}{-2x + 2y + 3}$$

$$lfb = \sqrt{(u - 0.292)^2} + \sqrt{(v - 0.24)^2} \qquad \textbf{Eq. (9.2)}$$

The American National Standards Institute (ANSI) recommended the value of Duv lie between the ± 0.006 tolerances for white light. In our study, the Cu(II) complex has positive values with a bluish-green tinge, and the remaining two have negative values with a slightly pinkish shade. The tolerance level of Cu (II) ion is much greater than white light. The color consistency Δu'v' and its stability present only the magnitude and not the direction of the change. All three sources started at a uniform chromaticity point but lifted opposite, as shown in **Figure 9.12 b** and **Table 9.8**.
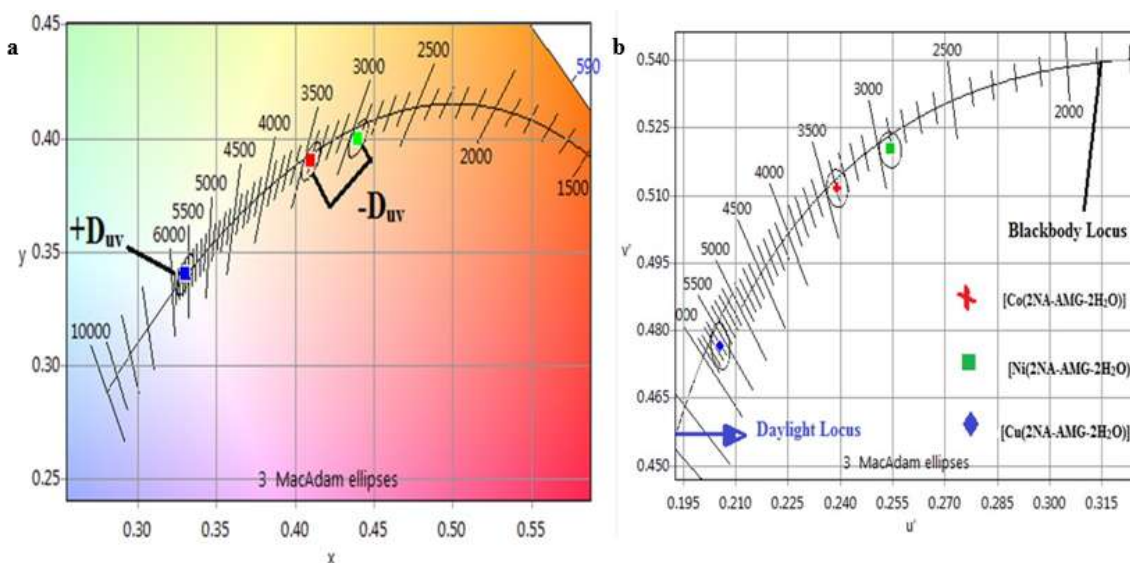
Figure 9.12 *a)Correlated Color Temperature was determined using Planckian locus b) color consistency and its stability was evaluated using Δu'v'*

Table 9.8 *Duv metric is evaluated with the help of CIE 1931*							
Samples	**CCT(K)**	**U'**	**V'**	**DuV**	**Du'v'**	**Ldom (nm)**	**Purity (%)**
[Co(2NA-AMG)]	3312	0.2391	0.2391	-0.0013	-0.0019	581.8	40.1
[Ni(2NA-AMG)]	2833	0.2543	0.5202	-0.0020	-0.0029	583.9	52.1
[Cu(2NA-AMG)]	5278	0.2056	0.2056	0.0006	0.0007	521.6	1.3

9.4.3.3 Color Rendition Metrics

CRI, referred to as the CIE test color method, was used to differentiate the color rendering effect of a new light source compared with the traditional one. CRI is an important grade for fluorescent tubes since they are missing portions of the spectrum and talk about the difference's magnitude. The light sources with similar CRI values will render different colors [4].

The primary metric of the CIE is Ra, which was determined from the average value of the first eight colors and typically ranges from 0 to 100; even negative values are possible. For the copper complex **(Figure 9.13 a-b)** Ra =87, which means that it can be used for workplace lighting and high-quality light applications, but for Ni(II) and Co(II) complexes, we are getting negative values. In addition, for the copper (II) complex, the % CRI is 90, confirming the above statement **(Table 9.9)**.
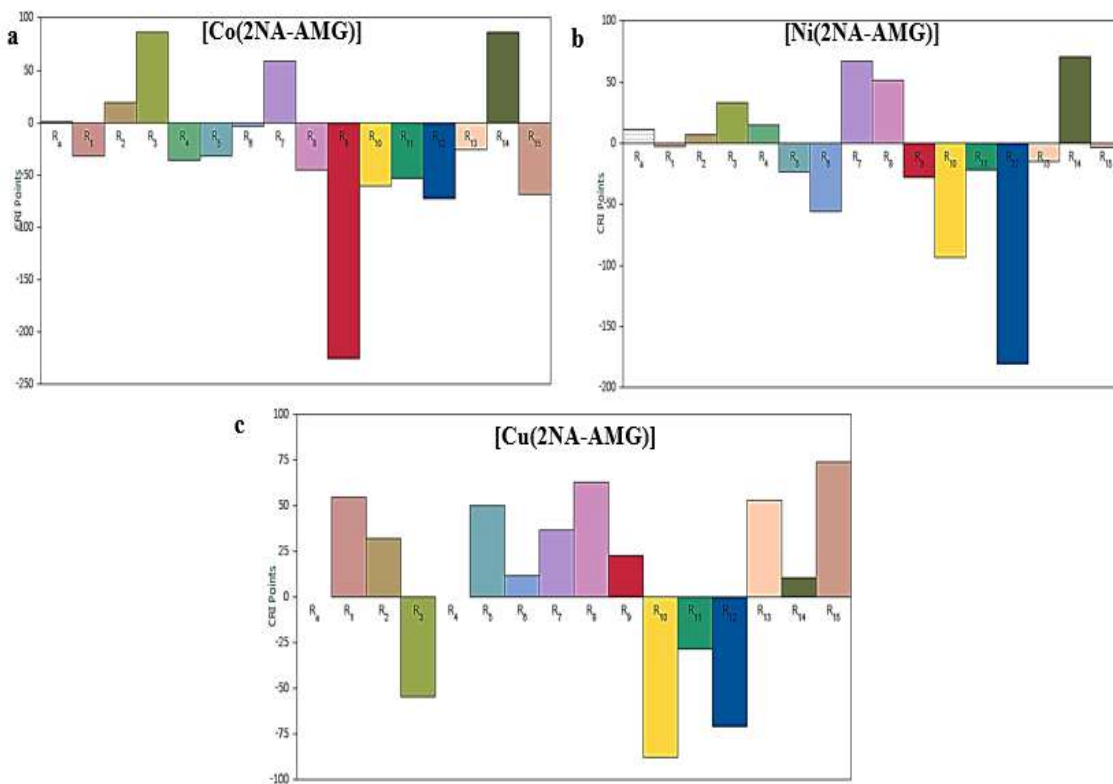
Figure 9.13 *Color Rendition Metrics a) Co(II) b) Ni (II) and c) Cu (II) complexes*

Table 9.9 *Color rendering index (CRI) measured from R1 to R15 of the optimal WLED lamp*

Samples	R1	R2	R3	R4	R5	R6	R7	R8	R9	R10	R11	R12	R13	R14	R15
[Co(2NAAMG)]	-3	7	34	15	-24	-56	68	52	-28	-94	-22	-181	-15	71	-4
[Ni(2NA-MG)]	-32	20	87	-36	-32	-4	60	-45	-225	-61	-53	-73	-26	87	-69
Cu(2NA-AMG)]	55	32	-55	0	50	12	37	63	23	-88	-29	-71	53	11	74

9.4.3.4 TLCI (Television Lighting Consistency Index)

The EBU - European Broadcasting Union established the Television Lighting Consistency Index (TLCI), a novel assessment standard for studio lights for the TV and film industry. TLCI uses the standard set of color test samples & correlates the image in the light source (test) with black-body radiation reliant on the color temperature. TLCI determination doesn't include a test chart & video camera; preferentially, the complete test was carried out using mathematically modeled software [5].

The TLCI value and their observation for our target molecules are as follows

i.   Co(II) – 72 A colorist would definitely need to modify the errors and could perhaps accomplish a satisfactory effect; however, it needs considerable time. It is usable but requires correction in the video chain setup.

ii. Ni(II)- 28 The color rendering is reduced and cannot be usable, even when a correction is made. This is not a good source for video or television applications.

iii. Cu(II) – 100 indicates that this light source is extensively viewed for television use.

Figure 9.14 (a-b) shows the Color Checker chart, which displays every patch with an outer band (reference light source) and inner band (test source). At the bottom right, the spectra of the reference radiation source were shown in cyan, and the test light source, in black. The two peaks of the RGB (red, green, blue) light source are seen in the bottom right corner of the image. The top right corner of the color chart displays the predictable correction that should be utilized in the video chain to fetch the image into the transmission. For the Co(II) complex, it takes a large quantity of shade and color rectification, and it travels in the region of magenta blue & magenta red to fetch the tinge posterior within the

border. For Ni(II) at 5633 K, there is a bundle of vanished energy in the hue region; in addition, it stretches from blue to magenta red. Cu(II) proves how LED can do good work with phosphors. The TLCI value is 100 and needs no camera corrections and single narrow peak tails from the blue color.

Figure 9.14 *Television Lighting Consistency Index for a) Co(II) b) Ni (II) and c) Cu (II) metal complexes*

9.5 APPLICATION USING NiO and CoO OXIDE TO ENHANCE THE CORROSION RESISTANCE

### 9.5.1 Preparation of Oxide Composite

NiO and CoO cations were synthesized by dissolving the $Ni(NO_3)_2 \cdot 6 H_2O$, and $Co(NO_3)_2. 6H_2O$ (0.290 g and 0.291g mmol each) 0.1721 g of 2-naphthoic acid and 0.136 g of aminoguanidine in 40 ml of (acetone/water 20 ml each) under vigorous stirring in a room environment. The reaction mixture was kept in a water bath and temperatures were maintained till the solution got half of its original solution. The resulting product was centrifuged (at 8000 rpm) and washed with ethanol several times and died under 30 °C in a vacuum. They were calcinated at muffle to form nanoparticles shown in **Figure 9.17**.

Figure 9.17 *Preparation of Oxide*

### 9.5.1.1 Vibrational spectra of metal oxide

The NiO and CoO oxide nanoparticles were calcinated at 800 °C as represented in **Figure 9.18a,b**. in which -OH shows a broad peak at 3433-3388 cm^{-1} that is attributed to the presence of water molecules. The stretching vibration between the metal and the oxygen confirms the formation of nanoparticles by a strong band around 610-705 cm^{-1}.
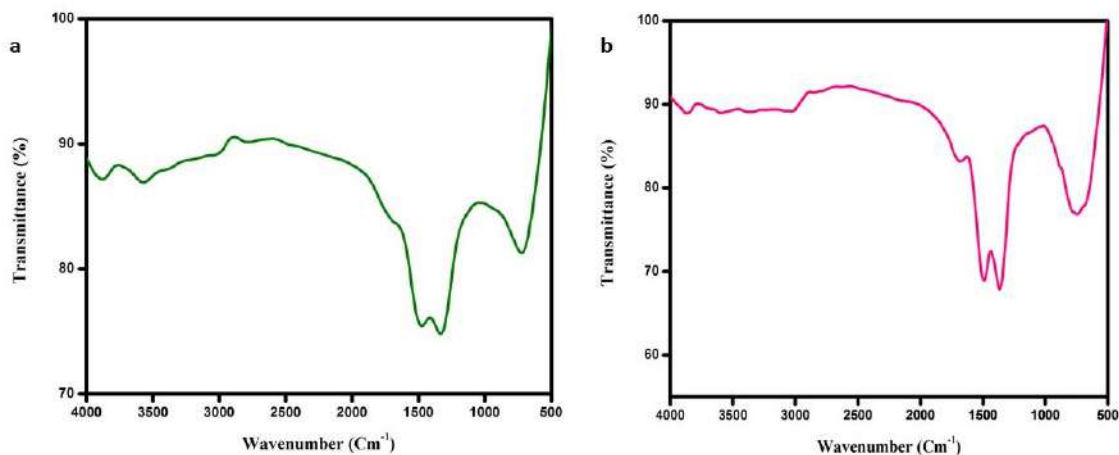
Figure 9.18 *FT-IR spectra of a) NiO b) CoO*

9.5.1.2 Electronic spectra of metal Oxide

Figure 9.19a illustrates the UV-vis absorption spectra. The broadening of the absorbance peak is due to the distribution of particle size. The optical energy was estimated from Tauc's plot which is shown in **Figure 9.18b**. From the electronic transition, the power factor for NiO and CoO oxide was found to be, 'n' value ½, and the energy gap was estimated as 2.9 eV for NiO and 3.2 eV for CoO [7].
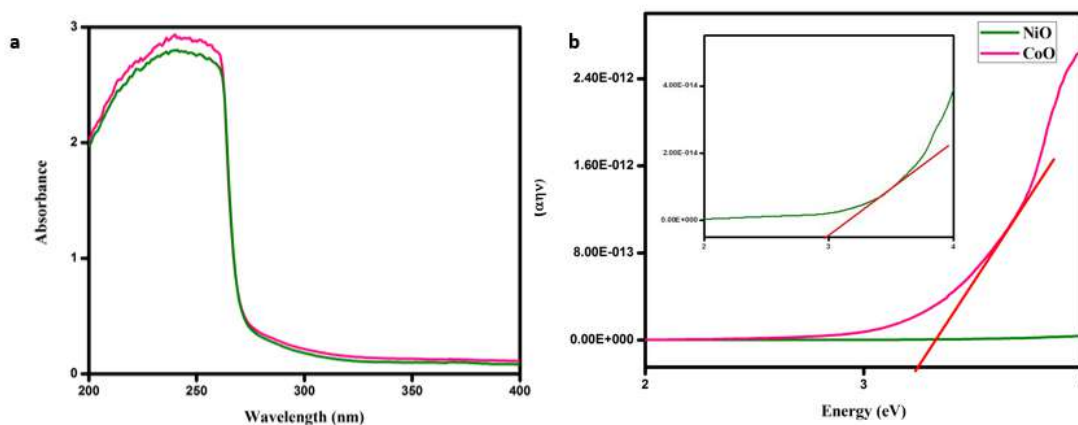
Figure 9.19 *UV-visible spectra of a) NiO and CoO b) Optical energy by Tauc's Plot*

9.5.1.3 Powder-XRD of Metal Oxide

The Powder-XRD examines the phase structure and purity of the compound. The metal oxide exposed well-resolved diffraction peaks represented in **Figure 9.20a**, in which they can be indexed and the peak corresponds to the plane of NiO and CoO oxide

structure. There are no additional peaks were observed which denotes that they were high-degree phase purity. The overall average crystallize size is 10 nm which was determined using the Scherrer formula.

$$\beta_{hkl} = \left(\frac{k\lambda}{D}\cos\theta\right) + 4\epsilon\tan\theta \qquad\qquad \textbf{Eq. (9.3)}$$

$$\beta_{hkl}\cos\theta = \left(\frac{k\lambda}{D}\right) + 4\epsilon\tan\theta \qquad\qquad \textbf{Eq. (9.4)}$$

where D represents the size of the crystallite in nm, K represents the shape factor, λ is an incident X-ray wavelength, β is the full-width, and q invades the angle. **Eq. (9.4)** represents the plot against $\beta\cos\theta$ vs. $\sin\theta$ and a straight line was obtained in **Figure 9.20b** [8].
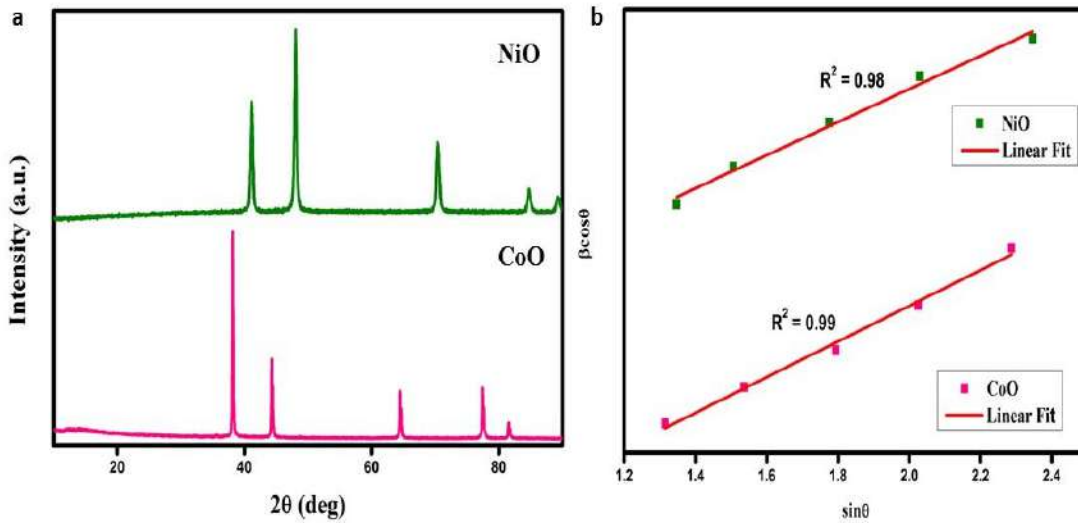
Figure 9.20 *Powder-XRD of a) NiO and CoO b) W-H UDM plot*

9.5.1.4 TG-DTA of Metal Oxide

Figure 9.21(a-b) represents the TG-DTA curve of NiO and CoO. Under a nitrogen atmosphere, the analysis was carried out at a temperature ranging from 0- 800 ° C. Between 0-100 ° C the adsorbed water was removed with a loss of 8 % and rapid loss occurred between 200-400 ° C, is due to the decomposition of organic moiety[9].
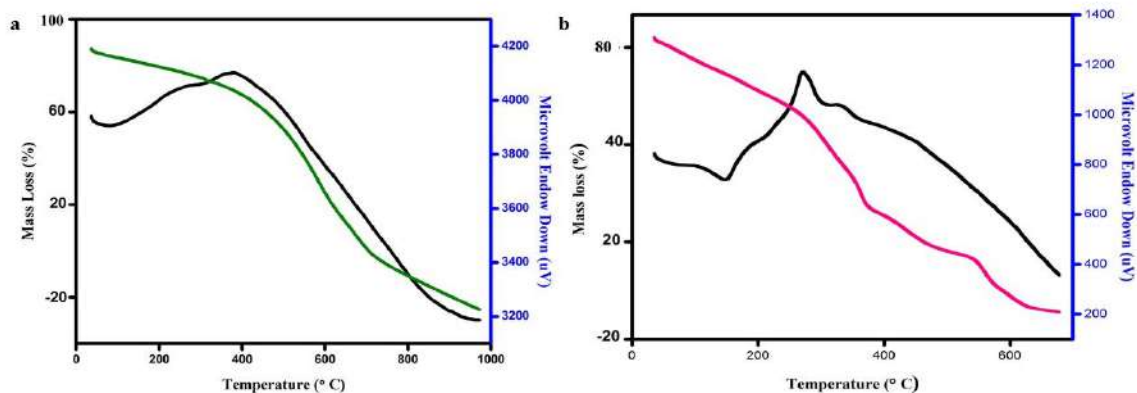
Figure 9.21 TG-DTA of a) NiO b) CoO Oxide

9.5.2 Morphological studies

Figure 9.22(a-b) reveals the FESEM image of NiO and CoO and shows a rock-like morphology. The metal complexes during the hydrothermal process get decomposed and then calcinated at 800 º C to form nanoparticles. The average size of the nanoparticles was found to be 10-12 nm. The EDS spectrum is represented in **Figure 9.22(c-d)** confirming the presence of Ni, Co, and O elements and the amount of the element present in the sample represented in **Table 9.12**. Element mapping demonstrates the dispersion between the nickel, cobalt, and oxide in **Figure 9.22(a-f)**.
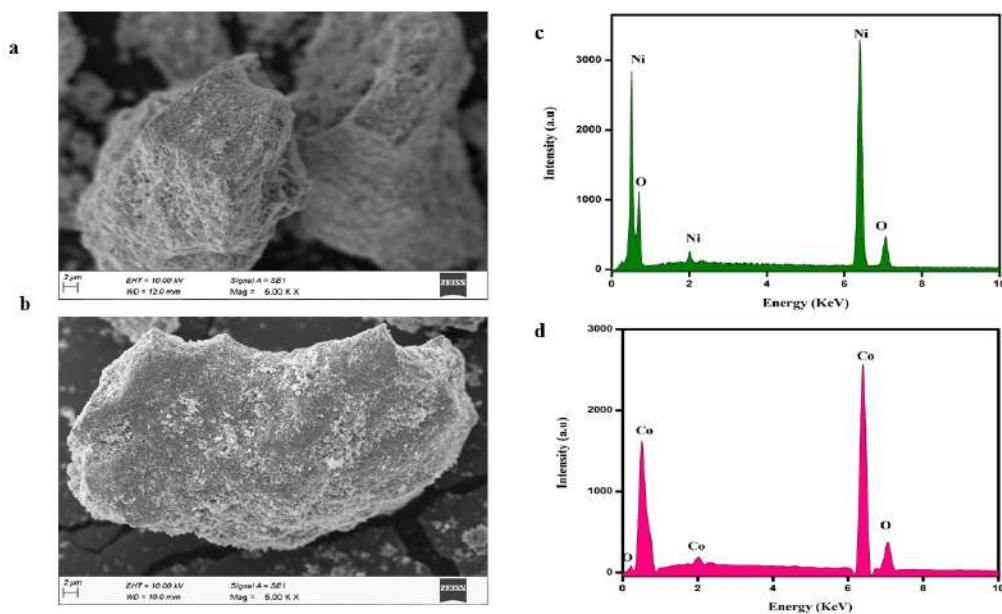
Fig 9.22 *(a,b)SEM image of Nickel Oxide and Cobalt Oxide (c,d) & EDS*
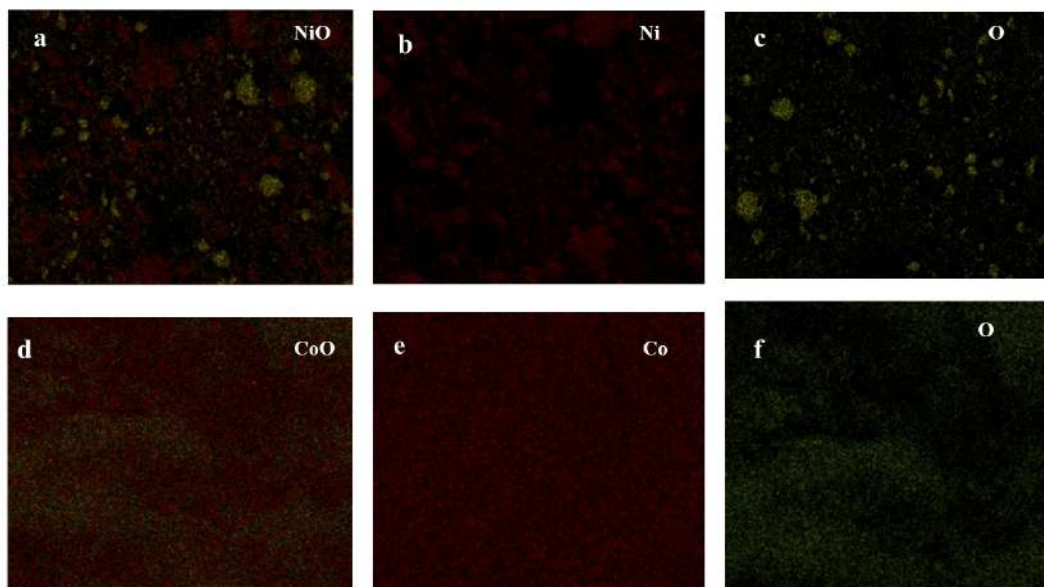
Figure 9.23 *(a-f) Element mapping Nickel Oxide and Cobalt Oxide*

Table 9.12 Element analysis		
Element	**Metal**	**Oxide**
NiO	68 %	32 %
CoO	67 %	33 %

9.5.3 Corrosion resistance

9.5.3.1 Bore water

The epoxy resin of NiO and CoO oxide was coated in the metal substrate are treated against the bore water in which sodium chloride was present in the solution at ranging from 5.1. The corrosion against the mild steel substrate exhibits various corrosion processes after 120 days. For blank, which contains only epoxy resin corrosion starts immediately **(Figure 9.24 a)** but with metal oxide, there is no evidence of corrosion even after 60 days after 120 days there is slight corrosion takes place which is shown in **Figure 9.24 (b& c)**. The formation of rust is seen as orange-red color which may be due to the formation of iron oxide. In general, CoO shows a good physical barrier and protects the steel plate from corrosion, compared with NiO and blank**.** The oxidation and reduction equation taking place at the steel substrate is shown below [10].

Reduction: $Fe \rightarrow Fe^{2+} + 2e^-$ **Eq. (9.6)**

Oxidation : $O_{2(g)} + 2H_2O + 4e^- \rightarrow 4OH^-$ **Eq. (9.7)**
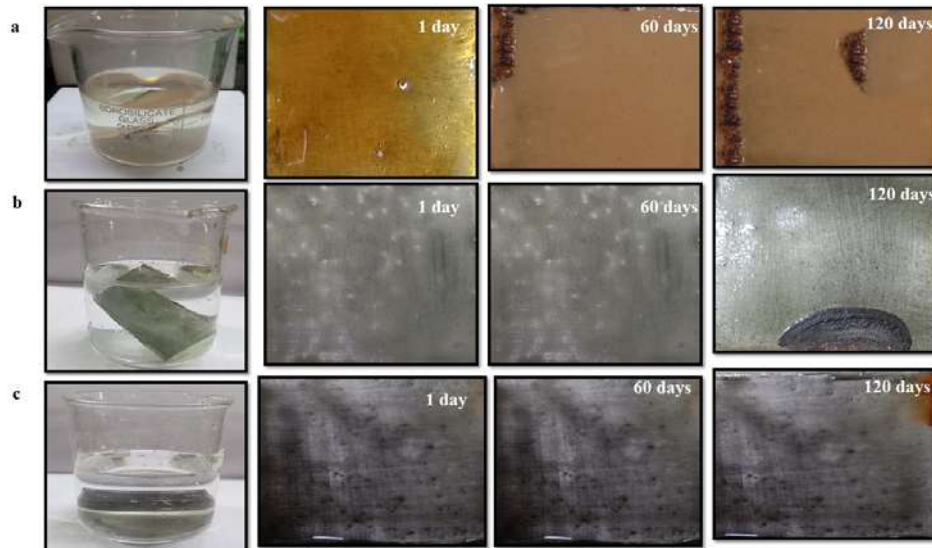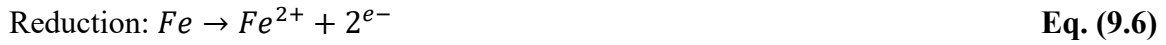
Figure 9.24 *(a-c) Corrosion resistance in bore water a) epoxy -Blank b) epoxy-NiO c) epoxy-CoO*

9.5.3.2 Soil corrosion

The sample was collected locally and sieved in 45μ size, where the pure sand was collected and oven-dried for 24 hours to remove the moisture content. The soil corrosion majorly depends on the amount of salt and acid content present in it. The macro images of the steel plates before and after immersion in soil up to 120 days (coated with epoxy resin (blank), and epoxy-resin with metal oxide) are represented in **Figure 9.25**. The plate with epoxy resin alone (blank) shows severe corrosion and the top layer was completely deteriorated **(Figure 9.25a).** The epoxy resin with nanometal oxide undergoes slow corrosion and compared with nickel oxide **(Figure 9.25b)**, cobalt oxide **(Figure 9.25c)** acts as a good inhibitor.
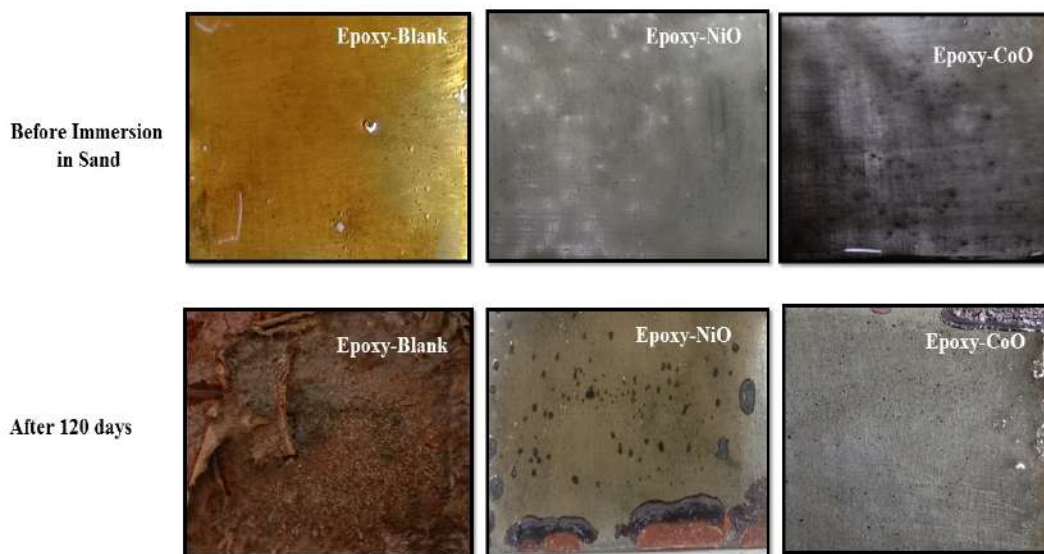
Figure 9.25 *Corrosion resistance in soil a) epoxy -Blank b) epoxy-NiO c) epoxy-CoO*

9.5.3.3 Antibacterial study

      Figure 9.28 represents the photographic image of the inhibition zone of a mild steel substrate coated with epoxy-NiO and CoO. The bacterial study was carried out against the gram(+) and gram (-). The mild steel specimen is represented in mm and illustrated in **Table 9.13.** The antibacterial activity against *Staphylococcus aureus* and *Escherichia coli* was also determined. The CoO shows higher inhibition against *Staphylococcus aureus* and *Escherichia coli* respectively. They were determined by the equation.

$$Percent\ reduction = \frac{(A-B)X\ 100}{A}$$
                 Eq.(9.8)

$A = Number\ of\ viable\ organism\ before\ treatement$

$B = Number\ of\ viable\ organism\ ater\ treatement$

Table 9.13 *Inhibition zone of NiO and CoO*		
Metal specimen	**Inhibitory Diameter (mm)**	
	G+ve **(E.coli)**	**G-ve** **(*B.subtilis*)**
NiO	0.3	0.2
CoO	0.4	0.3
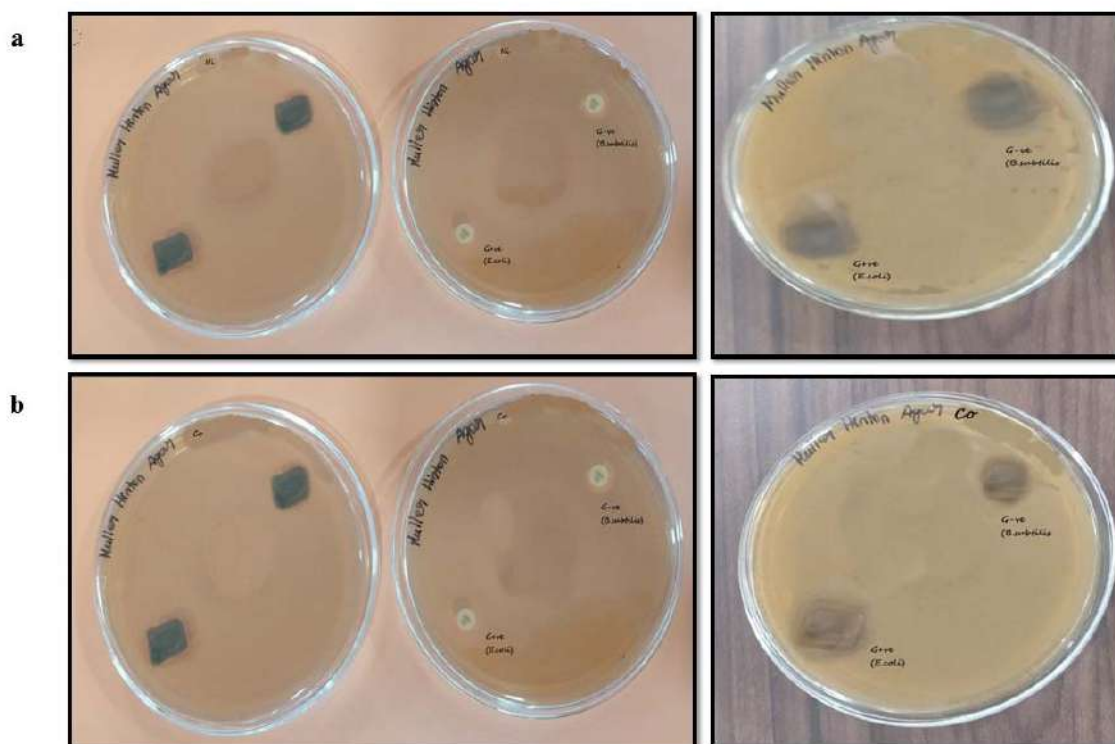
Figure 9.28 *Photographic image of the inhibition zone of a mild steel substrate coated with a) epoxy-NiO and b) epoxy-CoO*

9.5.3.4 Electrochemical impedance spectroscopy

The EIS is used to determine the electrochemical properties, corrosion protection, and ionic resistance in 3.5 wt % NaCl. The imaginary vs. real impedance, the bode plot, and the phase angle are illustrated in **Figure 9.29 (a-c)**. The bode plot (**Figure 9.29b**)

represents the Z value used to determine the corrosion resistance, the higher value specifies the corrosion rate is better on the steel substrate. **Figure 9.29c** is the phase angle diagram, which evaluates the resistance of corrosion and interfacial bond between the metal oxide and substrate. Compared with blank and epoxy-NiO, epoxy-CoO nanoparticles show better barrier activity against the metallic substrate.
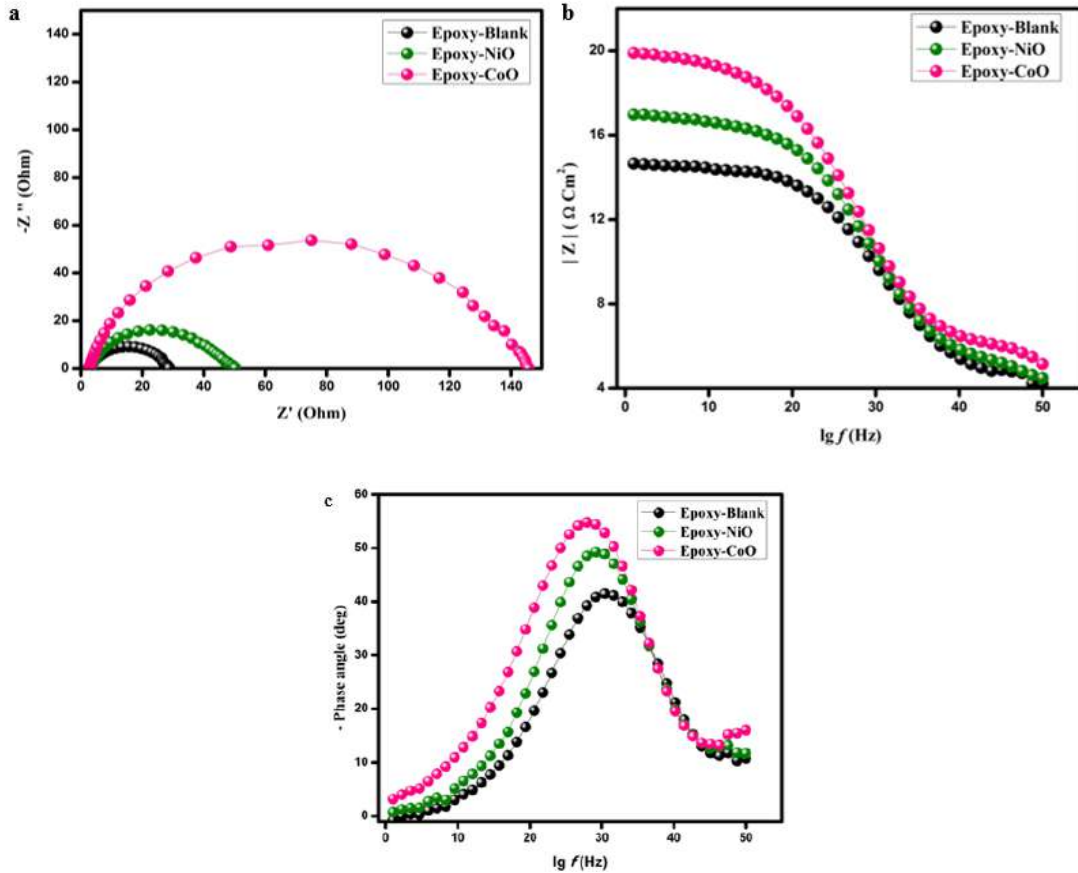
Figure 9.29 *EIS analysis a) Nyquist plot b) Bode plot C) Phase plot*

9.5.3.5 Polarization studies

The polarization curve for the blank, epoxy-NiO, and CoO was carried in a corrosion medium and was attained immediately after the EIS experiment. **Figure 9.30** shows a linear Tafel plot concerning anodic and cathodic areas. The electrochemical parameters of the polarization curve are represented by E_{corr}, the corrosion potential and the corrosion density are represented by i_{corr}, and the slopes b_a (anodic) and b_c (cathodic) values were observed and presented in **Table 9.14**. The Tafel curves are evaluated by the Stearn-Geary calculation.

$$R_p = \frac{\beta_a X \beta_c}{2.303 \, X \, (\beta_a X \beta_c) X \, i_{corr}}$$ **Eq.(9.9)**

E_{corr} shows the highest corrosion potential, i_{corr} represents the lowest corrosion, and the corrosion rate implies good barrier properties and a high corrosion rate. While comparing the blank, epoxy-NiO/ CoO, the epoxy-CoO produces less i_{corr}, and high E_{corr} which indicates the effective barrier property[12].
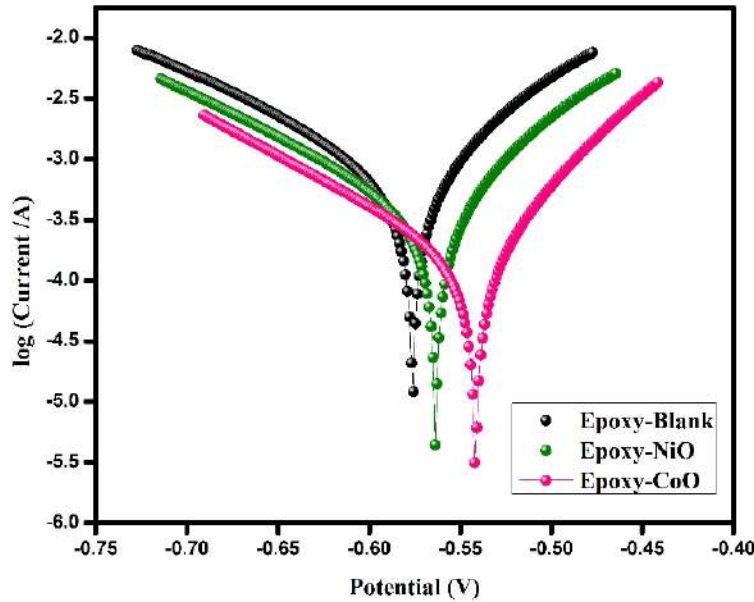
Figure 9.30 *Polarization curve*

CONC	ba	bc	Ecorr	Icorr	IE
Blank	138.7	86.4	-576.11	689.7	
NiO	137.5	78.4	-563.5	370.78	46.24
CoO	130.6	67	-541.6	102.8	85.09

Table 9.14 The corrosion potential and the corrosion density of potential polarization

9.5.3.6 Atomic force microscopy (AFM)

The 2D and 3D images of AFM represent the topography of the metal substrate and are shown in **Figure 9.31 (a-f).** The topography of epoxy-blank on the metal specimen exhibits deep stomas on the surface and the corrosion attack is large in which the highest

roughness occurred at 41.40 nm. For the metal specimen coated with epoxy-NiO/CoO, the corrosion attack was lesser than the epoxy-blank which is evident from the graph. The epoxy-NiO shows a small pit (23.08 nm) on the surface whereas the epoxy-CoO (1.46 nm) shows a smooth surface. This confirms the adsorption of the M-O on the surface and their activity towards the corrosion resistance[13].
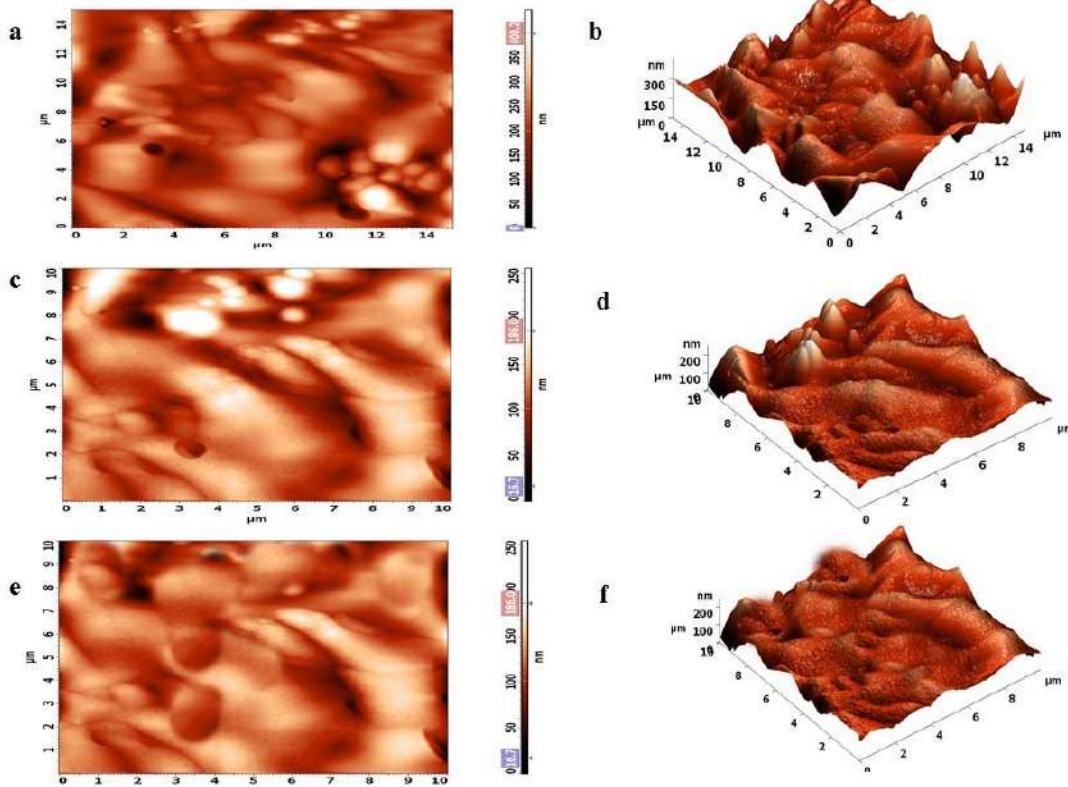
Figure 9.31 *AFM image (2D and 3D) (a,b) epoxy-blank (c,d) epoxy-NiO (e,f) epoxy-CoO*

9.5.3.7 Corrosion mechanism

The corrosion mechanism was determined from the rate of iron dissolution along with the presence of anions and the chlorine ions adsorbed on the metal surface. The precise corrosion mechanism is shown below:

$$Fe + Cl^- \rightarrow (FeCl)^- \qquad \text{Eq.(9.10)}$$

$$FeCl^- + H_2O \rightarrow FeOHCl^- + H^+ + e^- \qquad \text{Eq.(9.11)}$$

$$FeOHCl^- \rightarrow FeOHCl + e^- \qquad \text{Eq.(9.12)}$$

$$FeOHCl + H^+ \rightarrow Fe^{2+} + H_2O + Cl^- \qquad \text{Eq.(9.13)}$$
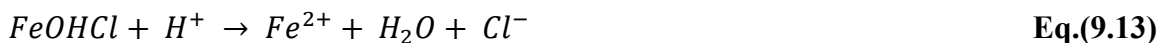
The corrosion mechanism explains the anti-barrier epoxy-NiO/CoO against the metal substrate shown in **Figure 9.32**. For, the epoxy blank the Cl^-, O^2, H_2O, and other corrosive species enter through the coatings easily due to the presence of free volume and micro-spores, which leads to the degradation of the metal **(Figure 9.32a)**, whereas with epoxy-NiO/CoO coating the surface pores are covered and the corrosive species do not have space to occupy on the surface of the metal.

Hence the epoxy-NiO/CoO coating which shows a corrosion barrier against the steel increases the hydrophobicity on the steel surfaces [14].
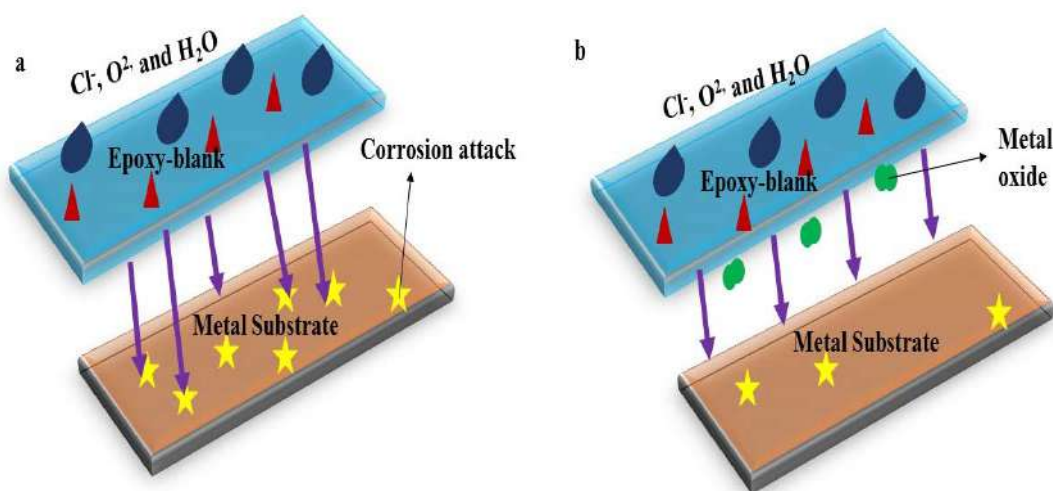
Figure 9.32 *Schematic corrosion mechanism a) Blank b) With* epoxy-NiO/CoO

9.6 CONCLUSION

A series of novel $[M(C_2H_7N_4O_3)_2\{C_{10}H_7(COO)\}_2.2H_2O]$ complexes with naphthoic acid and aminoguanidine have been synthesized, and characterized. FT-IR confirms the presence of functional groups and monodentate linkage of the ligands. P-X-ray diffraction was well-defined, and sharp peaks indicate the crystalline nature of the complexes. UV-visible spectra indicate the π-π* and the n-π* transition at a longer wavelength and authenticate the presence of distorted octahedral geometry around the metal ion. TG-DTA confirms the thermal stability and shows dehydration and decomposition are the major mechanistic processes. The final decomposition was concerned as metal oxides arise from the 500° C – 800 °. Antimicrobial activity shows good inhibition for Zn (II) complex.

The metal complexes are found to be promising aspirants as phosphorescent materials for OLED applications. In photoluminescence spectra, cobalt moiety shows enhanced spectra due to the MLCT process. The decay lifetime was in the range of 525 μs which establishes the luminescence character of the title compound. In correlated color temperature, the Cu(II) complex shows positive values with bluish green tinge while others have negative values with a slightly pinkish shade. The tolerance level of Cu (II) ion is much greater than white light compared with American National Standards Institute standard values. The color rendering index and TLCI for the copper complex are high with a 90 %CRI value, proving this complex's promising application in workplace lighting and television. The photometric properties of synthesized complexes have been examined in a substantial range owing to their thermal stability, cost-effective synthetic procedure, and progressive applications as white phosphors.

The metal oxides synthesized from complexes were characterized by FT-IR, UV-visible spectra, TG-DTA, and P-XRD. The FT-IR signifies the formation of M-O around 610-705 cm^{-1}. The optical energy was predicted from Tauc's plot and the energy gap was estimated as 2.9 eV for NiO and 3.2 eV for CoO. Powder-XRD observes the phase structure and purity of the metal oxide. There are no additional peaks that denote the high degrees of phase purity. The average crystallization size is 10 nm. In TG-DTA the initial loss was found between 200-400 º C, due to the removal of water. DTA curve signifies an exothermic peak around 392-406º C due to the formation of pure NiO and CoO. FESEM resembled a flower-like structure and elemental mapping proves the dispersal between nickel, cobalt, and oxide. The corrosion resistance of metal oxide was studied in bore water, and soil. Based on the result epoxy-CoO shows good anticorrosive properties than epoxy-NiO due to the hydrophobicity on the metal substrate whereas epoxy-blank exhibits poor protection due to the diffusion pathway in the corrosive metal substrate.

REFERENCES

1. N.Arunadevi & S.Vairam. Preparation of transition metal 2-hydroxy-1-naphthoate complexes with hydrazine, their thermal characterization, and use as precursors of nano metal oxides. *Inorg. Chem. An Indian J.* **4**, (2009).

2. Wang, G. H., Li, Z. G., Jia, H. Q., Hu, N. H. & Xu, J. W. Metal–organic frameworks based on the pyridine-2,3-dicarboxylate and a flexible bispyridyl ligand: syntheses, structures, and photoluminescence. *CrystEngComm* **11**, 292–297 (2009).

3. Nagaveni, V. B. *et al.* Synthesis, crystal structure and excellent photoluminescence properties of copper (II) and cobalt (II) complexes with Bis(1[(4-butylphenyl)imino]methyl naphthalen-2-ol) Schiff base. *J. Sci. Adv. Mater. Devices* **3**, 51–58 (2018).

4. Smet, K. A. G., Whitehead, L., Schanda, J. & Luo, R. M. Toward a Replacement of the CIE Color Rendering Index for White Light Sources. *LEUKOS - J. Illum. Eng. Soc. North Am.* **12**, 61–69 (2016).

5. Böhler, P., Emmett, J. & Roberts, A. Toward a 'standard' television camera color model. *SMPTE Motion Imaging J.* **122**, 30–36 (2013).

6. Tadavi, S. K., Yadav, A. A. & Bendre, R. S. Synthesis and characterization of a novel schiff base of 1,2-diaminopropane with substituted salicyaldehyde and its transition metal complexes: Single crystal structures and biological activities. *J. Mol. Struct.* **1152**, 223–231 (2018).

7. Racik, K. M., Joseph, M. & Raj, V. A. Synthesis , Characterization and Optical Properties of Spherical NiO Nanoparticles. *Natl. Laser Symp.* (2018).

8. Nath, D., Singh, F. & Das, R. X-ray diffraction analysis by Williamson-Hall, Halder-Wagner and size-strain plot methods of CdSe nanoparticles- a comparative study. *Mater. Chem. Phys.* **239**, 122021 (2020).

9. Emamdoust, A., Farjami Shayesteh, S., Arvand, M. & Sayar, M. The effect of an anionic surfactant on structure and supercapacitive properties of flower-like nickel oxide. *J. Mater. Sci. Mater. Electron.* **29**, 17722–17730 (2018).

10. Liu, P. *et al.* Advanced corrosion resistant cylinder-bore coatings. *IOP Conf. Ser. Mater. Sci. Eng.* **1147**, 012034 (2021).

11. Chen, C. *et al.* A review of fluorescence based corrosion detection of metals. *Corros. Commun.* **6**, 1–15 (2022).

12. Kang, D. W. & Lee, H. W. Study of pitting resistance of duplex stainless steel weldment depending on the Si content. *Int. J. Electrochem. Sci.* **9**, 5864–5876 (2014).

13. Azani, N. F. S. M. & Hussin, M. H. Comparison of cellulose nanocrystal (CNC) filler on chemical, mechanical, and corrosion properties of epoxy-Zn protective coatings for mild steel in 3.5% NaCl solution. *Cellulose* **28**, 6523–6543 (2021).

14. Wang, C. *et al.* Anti-corrosive and scale inhibiting polymer-based functional coating with internal and external regulation of TiO2 whiskers. *Coatings* **8**, (2018).